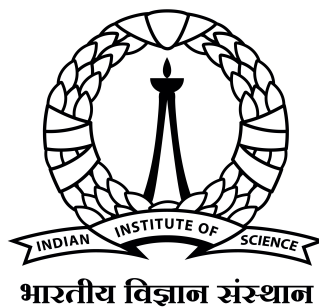


CRITICAL ANALYSIS OF SHARP PHASE FIELD METHOD

A THESIS SUBMITTED FOR THE DEGREE OF
MASTER OF TECHNOLOGY
IN THE FACULTY OF ENGINEERING

BY

AKSHITH YALALA



DEPARTMENT OF MATERIALS ENGINEERING
INDIAN INSTITUTE OF SCIENCE
BANGALORE - 560 012, INDIA
JULY 2022

Acknowledgements

I wish to express sincere gratitude to my advisor Prof. T.A.Abinandanan whose guidance and support in academic and personal matters helped me immensely. His vast knowledge, enthusiasm and welcoming nature helped me immensely while working on this project. I would like to thank all the professors whose teachings made me to enjoy learning at IISc. I also would like to thank Prof. Abhik N Choudhury whose courses on modelling piqued my interest to work in this area.

I also thank my lab mate Jitin Nair for helping me to code more efficiently and making my work on the project easier. I will always look forward to our intense discussions about all things under the sun. Lastly, I thank all my friends here at IISc who made my stay more memorable.

Abstract

Phase Field Modelling is a popular modelling technique for simulating different microstructural features. One limitation in phase field modelling is an artefact called numerical or grid pinning. A recent method called Sharp Phase Field Method (Sharp-PFM) developed by Finel et al. addresses the issue of numerical pinning and claims certain advantages over the regular phase field method. In this thesis the Sharp-PFM is analysed by employing it using Allen-Cahn and Cahn-Hilliard evolution equations and comparing its results with that of regular or classical phase field method (Classical-PFM).

The novelty of Sharp-PFM is that the free energy potential is derived from the assumed equilibrium profile equation for a given system unlike the Classical-PFM where a double well type of potential is assumed initially. There was no grid pinning observed when using the Sharp-PFM while its effect was seen in Classical-PFM.

In Allen-Cahn model, after matching the parameters across models, it is observed the Sharp-PFM shows very good kinetic accuracy which is only possible in Classical-PFM with a smaller grid spacing. It is also observed that Sharp-PFM took shorter simulation time with less memory requirement than Classical-PFM. So, Sharp-PFM with Allen-Cahn evolution is advantageous both in terms of memory and simulation time.

Using Cahn-Hilliard model, with similar interface energy and atomic mobility, it is observed that Sharp-PFM had smaller critical wavelength in spinodal decomposition and higher growth rate during growth of precipitate, compared to Classical-PFM. In 2D coarsening studies we were able to study coarsening using Sharp-PFM with a higher grid spacing than Classical-PFM, giving a good memory advantage. The maximum Δt in Sharp-PFM was smaller, making the simulation time same as Classical-PFM. So, Sharp-PFM with Cahn-Hilliard evolution is useful to study coarsening with higher number precipitates in same number of grid points as Classical-PFM and also in simulations where memory is a constraint.

Contents

Acknowledgements	i
Abstract	ii
1 Introduction	1
2 Literature Review	4
3 Model Formulation	7
3.1 Classical Phase Field Model	7
3.1.1 Cahn Hilliard Equation for evolution of composition field	9
3.1.2 Allen Cahn Evolution	9
3.2 Sharp Phase Field Model	10
3.2.1 1D Formulation	10
3.2.2 2D and 3D Formulation	12
3.2.3 Cahn Hilliard Evolution	14
3.2.4 Allen Cahn Evolution	14
3.3 Non-Dimensionalisation	14
3.4 Numerical Scheme	15
3.4.1 Classic PFM - Cahn Hilliard	15
3.4.2 Classic PFM - Allen Cahn	16
3.4.3 Sharp PFM - Cahn Hilliard	16
3.4.4 Sharp PFM - Allen Cahn	17
3.5 Interfacial Energy Calculation	18
4 Results and Discussion	20
4.1 Grid Pinning	20
4.1.1 Classic PFM	20
4.1.2 Sharp Phase Field Method	21
4.2 Matching Interfacial Energy	23

4.2.1	Ponderation Coefficients	24
4.3	Allen Cahn Comparison	24
4.3.1	1D Comparison	24
4.3.2	2D Curved Grain Motion	25
4.4	Cahn Hilliard Comparison	30
4.4.1	Early Stage Spinodal Decomposition	30
4.4.2	1D Growth	34
4.4.3	2D Coarsening	37
4.5	Limitations	44
5	Conclusions	45
6	Future Work	46
A	Non-Dimensionalisation	47

List of Figures

1.1	Grid Pinning example	3
3.1	free Energy function in Classical Phase Field Model	8
3.2	Equilibrium composition profile in Classical Phase Field Model	8
3.3	Free energy function in Sharp-PFM Eq.3.14	11
3.4	Equilibrium order parameter profile in Sharp-PFM	11
3.5	A square 2D lattice	13
4.1	1D interface motion in Sharp-PFM	22
4.2	Equilibrium Profile of Sharp-PFM	23
4.3	Microstructural evolution in Allen Cahn evolution for Classical-PFM, with $\Delta x = 0.5$, and Sharp-PFM, d/w=1, at different time steps.	27
4.4	Comparison of R^2 vs time in Allen-Cahn evolution across different models	29
4.5	Variation of wavelength with time in Classical-PFM	31
4.6	Wavelength Distribution in Classical-PFM at time 50	31
4.7	Variation of wavelength with time in Sharp-PFM	32
4.8	Wavelength Distribution in Sharp-PFM at time 20	32
4.9	Variation of order parameter values with time in Classical-PFM	33
4.10	Variation of order parameter values with time in Sharp-PFM	33
4.11	Variation of $\frac{\partial^2 f}{\partial c^2}$ with composition in Classical-PFM	35
4.12	Variation of $\frac{\partial^2 f}{\partial \phi^2}$ with ϕ in Sharp-PFM	35
4.13	Theoretical and numerical growth rates in PFM and S-PFM	36
4.14	Microstructural evolution during coarsening for V_f of 0.2 in Classical-PFM and Sharp-PFM at different time steps.	38
4.15	Volume fraction vs Time for PFM and Sharp-PFM	39
4.16	$N^{-3/2}$ vs Time for PFM and Sharp-PFM	39
4.17	R^3 vs Time for PFM and Sharp-PFM	40
4.18	Radius vs Time for Classical-PFM for different chemical potential	41
4.19	Radius vs Time evolution in Classical-PFM ($\Delta x = 1$) and Sharp-PFM ($\Delta x = 2$)	42

- 4.20 Microstructural evolution during coarsening for V_f of 0.25 in Classical-PFM ($\Delta x = 1$) and Sharp-PFM ($\Delta x = 2$) at different time steps. 43

List of Tables

4.1	Average interface energy and amplitude of variation of interface energy during motion of interface in Classical-PFM for a Δx	21
4.2	Average interface energy and amplitude of variation of interface energy during motion of interface in Sharp-PFM for a Δx	21
4.3	Interface Energy and width variation with grid spacing in PFM	23
4.4	Interface Energy for a given and d/w in Sharp-PFM matching with PFM	24
4.5	Parameters for Allen Cahn Evolution in 1D	25
4.6	Mobility Values from 1D Allen-Cahn simulations	25
4.7	Mobility Values from 2D simulations	26
4.8	Error percentage between slope of R^2 vs time profile of a numerical model and analytical slope	28
4.9	Model parameters in 1D Spinodal Decomposition Simulation	30
4.10	Growth rates for Classical and Sharp PF models for different c_∞	36
4.11	Rate constants in coarsening simulation	40

Chapter 1

Introduction

The study of microstructures of materials is of great importance as it affects many properties of the material be it mechanical, electrical, magnetic or optical properties. The spatial arrangement of atoms and other defects constitutes the microstructure of a material. One of the ways of studying microstructural evolution is by employing modelling and simulation methods. Several methods are used in modelling in materials science such as density functional theory (DFT), Molecular Dynamics, Finite Element methods (FEM) and Phase Field methods (PFM).

The Phase Field methods have a unique advantage of defining an interface between two different features (phases) of a microstructure inherently in the formulation used to make the PF models. Whereas in other sharp interface methods like Finite Element method the interfaces have to be kept track of, which increases the mathematical complexity of models. Phase Field methods are thus used to study precipitate growth [1][2], solidification [3], grain growth [4] and other phase transformation phenomena [5] in materials science.

In Phase Field Models, an order parameter is used to define a phase which has two equilibrium values and the region between two phases contains values of order parameter between the two equilibrium values making a smooth transition from one phase to another. All the intermediate order parameter values constitute an interface. In order to solve the equations constituting these models we have to first discretise the model. While discretising it in space the chosen grid spacing decides the scale and resolution in the model. While working with systems on a larger scale (eg: in quantitative models [4]) the number of points required in system are very large and the grid spacing has to be chosen carefully considering the resolution required and total number of grid points in system. With a smaller grid spacing although the resolution improves it also increases the number of grid points which means more computation power required. With a larger grid spacing we can save on the scale of the computation but there can be a problem of

poor resolution and artificial grid pinning.

In PF models the interface is represented by a finite number of grid points depending on grid spacing. As this is quite often the smallest feature in a microstructure it would be beneficial to represent the interface with least number of possible points. One way to do this is to take a larger grid spacing and this is where we encounter artificial grid pinning which is a numerical phenomenon. In Classical-PFM when the grid spacing comes close to the interface width, then the interface velocity decreases and stops [6], which is referred to as grid pinning.

To understand the grid pinning we take a Phase Field model with two equilibrium phases having an interface. This system is represented by different grid spacing. As the system is let to evolve with a driving force, we can see that in system where grid spacing is larger ($\Delta x = 4$) the evolution stops after sometime and in system with $\Delta x=2$ the velocity reduces after sometime. In systems with $\Delta x <= 1$ the velocity is almost same and it does not stop until completion of evolution. In these PF models when the parameters, A and Kappa are unity, the analytical interface width is 4 [7] and in our model with grid spacing as 4 where the interface is being represented with essentially just a single point we can see the grid pinning phenomenon. Even in model where grid spacing is 2 and interface is being represented with 3-4 grid points there is slow down in the evolution.

A resent formulation introduced by Finel et al. [8] uses a new way of defining the free energy that can help us to represent the interface even with a single grid point without any effects of artificial grid pinning. This new approach is called Sharp Phase Field Method (S-PFM).

This new method of Sharp Phase Field Model (Sharp-PFM/S-PFM), which is recently developed method, has not been fully explored till now. The motivation for my current work is to use the formulation given by Finel et al. [8] to study the behaviour of this new model in Cahn Hilliard and Allen-Cahn evolutions to understand it's benefits more deeply compared to the Classical Phase Field Model (Classic-PFM/PFM). Also, look for any limitation that this method has which not been completely explored till now.

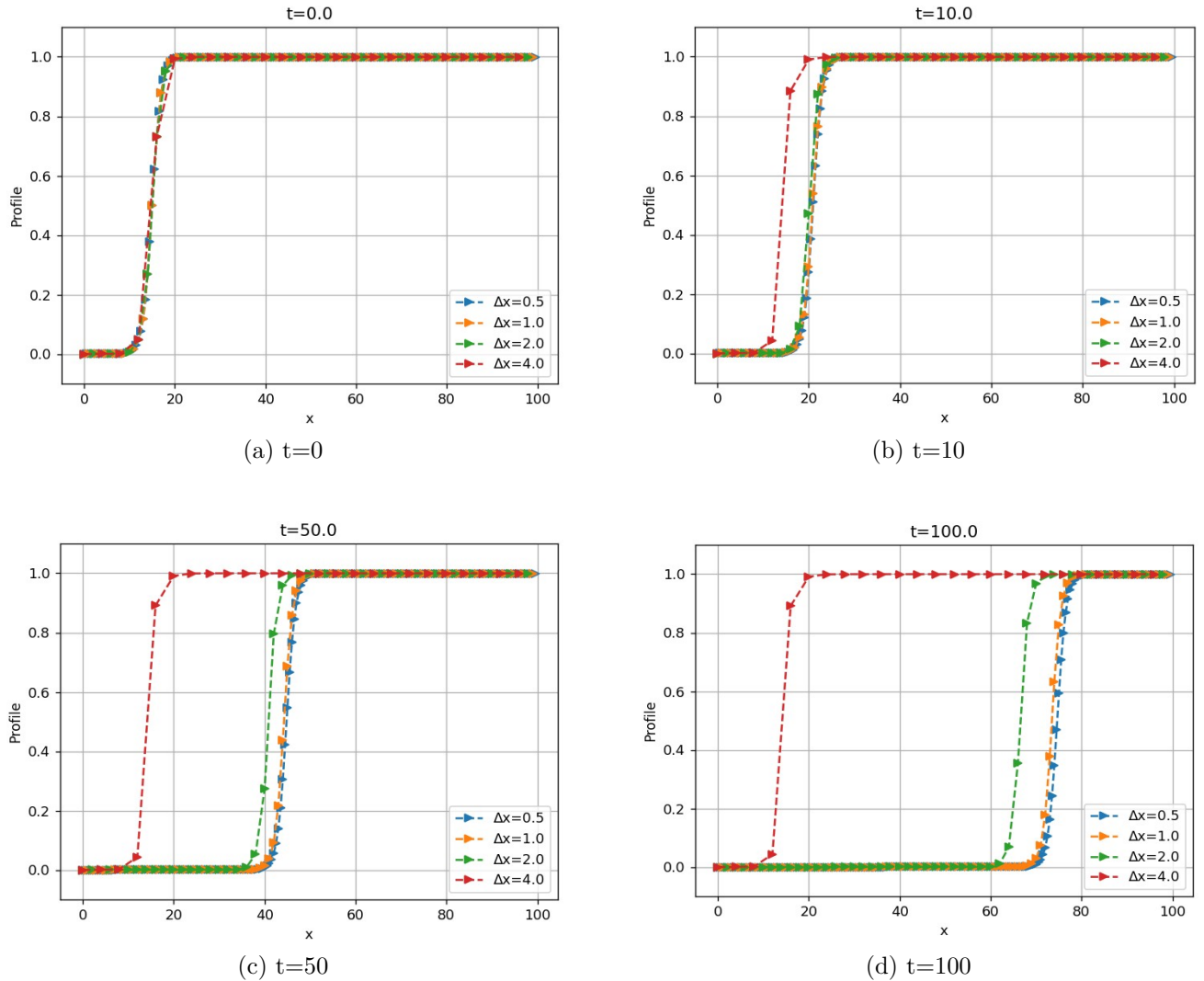


Figure 1.1: Grid Pinning example

Chapter 2

Literature Review

The concept of a diffuse interface between two equilibrium phases and its formulation is given by Cahn and Hilliard in [9]. They have calculated the interface energies of certain systems and their results closely matched the experimental observations. They developed this theory for isotropic interfaces and calculated the theoretical interface widths in a system. This chapter contains the theoretical background of Cahn Hilliard model and how it is adapted by others for working on different problems of metallurgy. The formulae from the Cahn and Hilliard's work are given in next chapter. The Free energy equation in Cahn Hilliard model contains energy contribution from local composition and the composition gradient. These two factors decide the interface energy and also the interface width in system. The gradient energy factor makes the system want to have a small gradient, and hence a wider interface. But, the points in such an have intermediate values of composition with a high energy, and this makes the system to preferentially have a narrow interface. For a given combination of these two opposing forces which is the minimum energy the system attains is the interface energy. These two parameters also decide the equilibrium interface width and profile.

Cahn [10] extended this model to study the evolution of composition field by proposing a relation between flux and chemical potential. This type of equation is called Cahn-Hilliard Evolution equation which deals with conserved order parameter, composition here. In all PF simulations using conserved parameter such as precipitate coarsening, spinodal decomposition the Cahn-Hilliard evolution equation is employed.

To study the evolution of systems where there is a continuous variation of non-conserved order parameter an evolution equation called Allen-Cahn evolution equation is used [11]. Modelling of grain growth, atomic ordering in system, phase transformations employ the Allen-Cahn evolution equation. Many microstructural transformations involve either the conserved or non-conserved order parameter evolution and many times a combination of both as well. A model where both type of parameters are involved is

studied by Khachaturyan et al. [12] where they showed simultaneous ordering and decomposition happening in the system. The system initially precipitates into an ordered state and then the decomposition happens in the ordered state.

Another study by Mukherjee et al. [13] showed the effect of misfit strain and interface curvature on precipitate growth where they have also used a free energy which is a combination of conserved and non-conserved order parameters. They show that interface curvature has a higher dampening effect on growth rate in particles of smaller size and low supersaturation and high misfit in system decreases growth rate.

Several studies [14] [15] have examined the effect of diffuseness of boundary on the velocity of a moving interface. By multiplying a coefficient to the potential energy and varying it the diffuseness of boundary is increased or decreased. With these changes in diffuseness, the velocity of a moving profile is calculated and compared to analytical results. It is observed that when the number of points in the interface, i.e., more diffuseness, increases the kinetic accuracy of models while by reducing the diffuseness, i.e., reducing number of points of points in interface, the velocity slows down to a significant extent. If the interface is made less and lesser diffuse then there could arise a situation where the boundary stops moving completely.

Fan and Chen [16] show that with very high interfacial energy anisotropy during microstructures simulation some interfaces may have higher or lower width compared to other directions. This forces us to choose a grid spacing which represents even the lowest interface width effectively, thus increasing computational power requirement. Otherwise there is risk of numerical pinning. In some simulations when some particles in microstructure coalesce then due to a large change in interface widths the results obtained were erroneous. Here again the effect of numerical pinning is observed.

With the formulation introduced by Finel et al. [8] they claim to have no effect of grid pinning or numerical pinning even at very high grid spacing values while also able to represent the interface with just a single point. In this method the free energy functional is taken in the discretised form and a modified form of free energy potential curve which is still a double well type of curve is defined. The results of their bench marking simulations were very close to analytical relations even when interface was represented using a single point.

In a follow-up work, Finel et al.[4] used the Sharp-PFM to study ideal grain growth using multi-phase field approach. Using lesser number of grid points representing the interface they were able to achieve the same level of accuracy as can be achieved in Classic-PFM but with a higher grid spacing. Because of this they were able to also show

that the computation time has been decreased by a factor of $4D$ (D is the dimension of space in system).

Fleck et al. [6] introduced a modified form the Sharp-PFM given by Finel [8] and proved that the effect of numerical pinning is not present in Sharp-PFM even when interface is resolved with a single grid point. They also work on diffusion limited solidification in 3D and prove that a range of varying driving forces can be used with this modified formulation of Sharp-PFM. It is also worked upon in another follow-up work by Fleck et.al [17] where their new method allows for very efficient quantitative simulation of solidification.

Chapter 3

Model Formulation

3.1 Classical Phase Field Model

The functional form of classical phase field model is taken as

$$F = N_v \int [f(c) + K(\nabla c)^2] dV \quad (3.1)$$

where $f(c)$ (c or ϕ is the order parameter in system) is the free energy potential and K is the gradient energy coefficient. The free energy potential is defined as

$$f(c) = Ac^2(1 - c)^2 \quad (3.2)$$

The variational derivative is defined as

$$\frac{\delta F}{\delta c} = \frac{\partial f}{\partial c} - 2K\nabla^2 c \quad (3.3)$$

The chemical potential is defined as

$$\mu = \frac{\delta(\frac{F}{N_v})}{\delta c} \quad (3.4)$$

The equilibrium profile of classical Phase Field models is given by

$$c = \frac{\exp(\beta x)}{1 + \exp(\beta x)} \quad (3.5)$$

where $\beta = \sqrt{\frac{A}{K}}$

The variation of free energy potential and equilibrium profile is shown in Fig. 3.1 and Fig. 3.2 respectively.

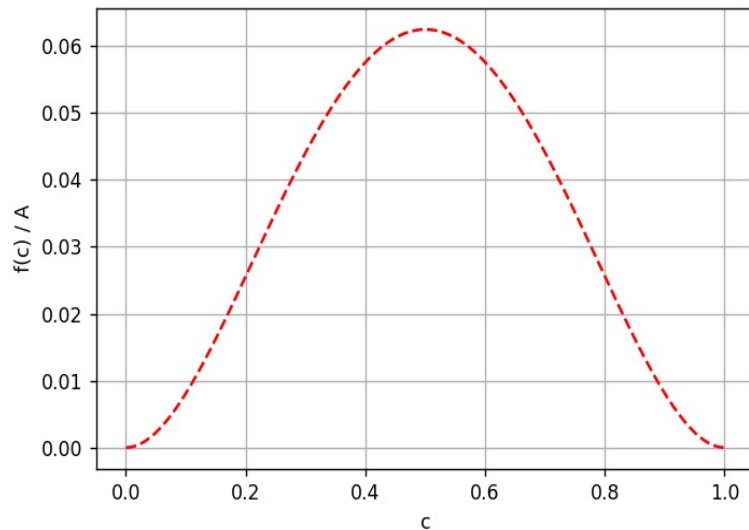


Figure 3.1: free Energy function in Classical Phase Field Model

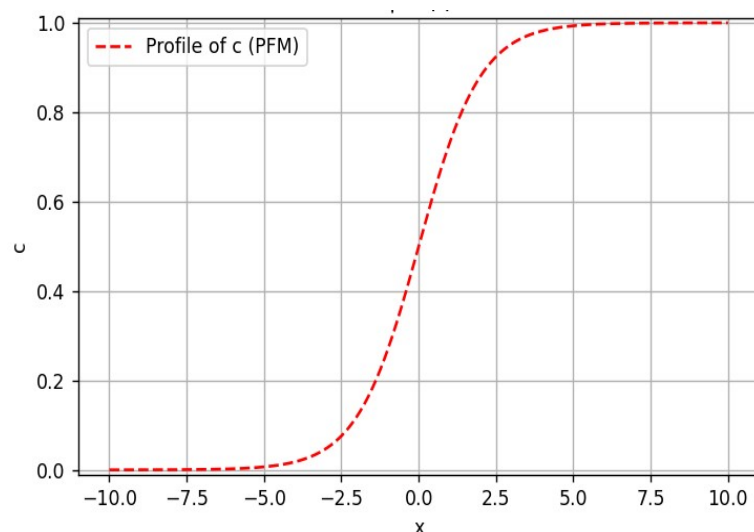


Figure 3.2: Equilibrium composition profile in Classical Phase Field Model

3.1.1 Cahn Hilliard Equation for evolution of composition field

Cahn Hilliard model is used for order parameters which are conserved, eg: composition. The Cahn-Hilliard model is thus defined as 3.6 and here M is atomic mobility parameter.

$$\frac{\partial c}{\partial t} = \nabla \cdot (M \nabla \mu) \quad (3.6)$$

with a constant M the expanded form becomes

$$\frac{\partial c}{\partial t} = M \nabla^2 \left(\frac{\partial f}{\partial c} \right) - 2KM \nabla^4 c \quad (3.7)$$

3.1.2 Allen Cahn Evolution

Allen Cahn model is used in modelling systems with non-conserved order parameters which is given by 3.8 . L in this equation is kinetic or relaxation coefficient.

$$\frac{\partial \phi}{\partial t} = -L \left(\frac{\delta F}{\delta \phi} \right) \quad (3.8)$$

on expansion this equation becomes

$$\frac{\partial \phi}{\partial t} = -L \frac{\partial f}{\partial \phi} + 2KL(\nabla^2 \phi) \quad (3.9)$$

3.2 Sharp Phase Field Model

In the sharp phase field the free energy is a discrete function instead of a continuous form of free energy functional in classical PFM.

3.2.1 1D Formulation

Starting with one-dimensional case the discrete free energy function is defined as

$$F = d \sum_n [f(\phi_n) + \frac{\lambda}{2d^2} (||\tilde{\nabla}\phi||)^2] \quad (3.10)$$

where d is grid spacing, n is coordinate point, $\tilde{\nabla}\phi_n = \phi_n - \phi_{n-1}$ and λ is the prefactor.

A discrete equilibrium profile between two phases is given by

$$\frac{\partial F}{\partial \phi} = 0$$

which gives

$$f'(\phi_n) - \frac{\lambda}{d^2} (\phi_{n+1} - \phi_n + \phi_{n-1}) = 0 \quad (3.11)$$

with boundary conditions $\lim_{x \rightarrow -\infty} \phi_n = 0$ and $\lim_{x \rightarrow \infty} \phi_n = 1$

The distinctive feature of Sharp Phase Field Model is that through equation 3.11 a free energy density profile $f(\phi_n)$ is now derived instead of assuming it as in classic phase field model. The way to define a $f(\phi_n)$ is that $\phi_n = g(nd)$ is solution to 3.11 and $\phi_n = g(nd - x_0)$ is also a solution to 3.11, because if this condition is satisfied then there is no grid pinning as the interface energy is now invariant by translation.

If $\phi_{(n+1)}$ and $\phi_{(n-1)}$ can be represented in terms of ϕ_n and x_0 is not present in the free energy potential equation then a solution that fits our requirements can be found more conveniently, one such example is

$$\phi_n = \frac{1 + \tanh(\frac{nd - x_0}{w})}{2} \quad (3.12)$$

From above expression we can write $\phi_{(n+1)}$ and $\phi_{(n-1)}$ in terms of ϕ_n as

$$2\phi_n \pm 1 = \frac{(2\phi_n - 1) \pm \alpha}{1 \pm (2\phi_n - 1)\alpha} \quad (3.13)$$

where $\alpha = \tanh d/w$

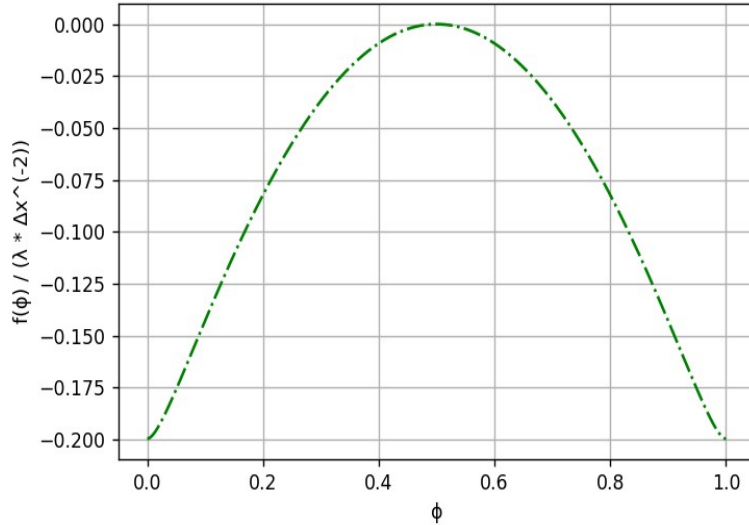


Figure 3.3: Free energy function in Sharp-PFM Eq.3.14

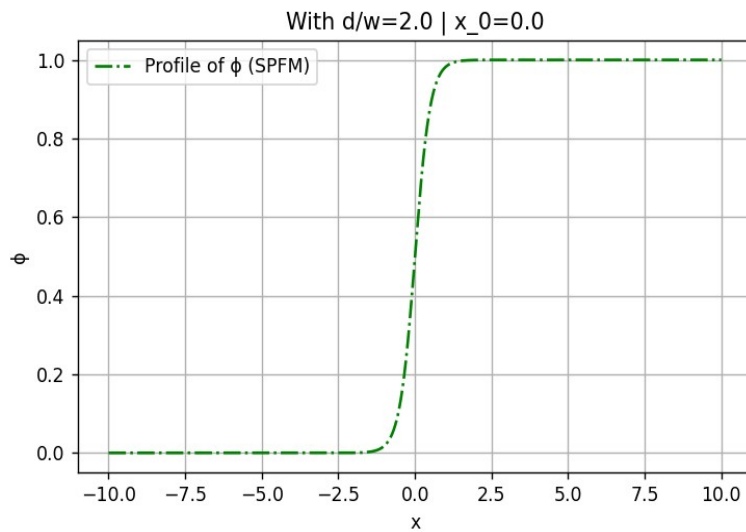


Figure 3.4: Equilibrium order parameter profile in Sharp-PFM

Using 3.11 and 3.13 we can write

$$\begin{aligned}
 f'(\phi_n) &= \frac{\lambda}{d^2} \left[\frac{(2\phi_n - 1) + \alpha}{1 + (2\phi_n - 1)\alpha} + \frac{(2\phi_n - 1) - \alpha}{1 - (2\phi_n - 1)\alpha} + 2 - 2\phi_n \right] \\
 f'(\phi_n) &= \frac{\lambda}{d^2} \left[\frac{1 - \alpha^2}{1 - \alpha^2(2\phi_n - 1)^2} - 1 \right] (2\phi_n - 1) \\
 f(\phi_n) &= \frac{\lambda}{4d^2} \left[\frac{\alpha^2 - 1}{\alpha^2} \log(1 - \alpha^2(2\phi_n - 1)^2) - (2\phi_n - 1)^2 \right]
 \end{aligned} \tag{3.14}$$

Eq. 3.14 is the free energy potential equation of Sharp Phase Field Model and it also has a double well potential given in Fig. 3.3 and the equilibrium profile is given in Fig. 3.4 based on Eq. 3.12. λ now represents the height of the free energy function in Sharp-PFM.

In the free energy potential and equilibrium formulation of the Sharp-PFM the parameter 'w' controls the width of the interface that will be formed. With the diffuseness/sharpness of the interface and the number of points inside it can be controlled. Hence, the name 'Sharp Phase Field Model'.

3.2.2 2D and 3D Formulation

It is not as straight forward to define a free energy potential in higher dimensions compared to 1D case. In order to derive a free energy density formula in higher dimensions we initially consider a lattice plane on the computational grid. Let us refer to this lattice plane as $(h_1 k_1 l_1)$, now we will construct a free energy potential $f(\phi)$ that has an invariant interface energy in direction perpendicular to $(h_1 k_1 l_1)$. Now two other lattice planes are selected, say $(h_2 k_2 l_2)$ and $(h_3 k_3 l_3)$. As interface energy will not be invariant across these two planes, the interface energies across these two planes are defined as the average of extreme values the interface energy reaches when an interface moves perpendicularly in that direction.

To derive the potential energy formula we proceed in a way to get equal interface energy in all three directions, thus making interface energy invariant, and this condition leads to the formula

$$\frac{F}{V_0} = \sum_{\vec{r}} \left\{ f(\phi(\vec{r})) + \frac{\lambda}{2} \sum_{i=1}^3 \gamma_i \frac{\nu_i}{d_i^2} \sum_{k=1}^{m_i} \|\phi[r + \vec{r}_i(k)] - \phi(\vec{r})\|^2 \right\} \quad (3.15)$$

By following the same procedure as in one-dimensional case the free energy potential is derived as

$$f(\phi) = \frac{\lambda}{4} \sum_{i=1}^3 \gamma_i \frac{\nu_i}{d_i^2} \sum_{k=1}^{m_i} \left\{ \frac{\alpha_i(\vec{r}_i(k))^2 - 1}{\alpha_i(\vec{r}_i(k))^2} \log(1 - \alpha_i(\vec{r}_i(k))^2(2\phi - 1)^2) - (2\phi - 1)^2 \right\} \quad (3.16)$$

here $\alpha_i(\vec{r}_i(k)) = \frac{\tanh \vec{r}_i(k) \cdot \vec{u}}{w}$, V_0 is volume per node in lattice, i represents i^{th} neighbor shell, and k runs over all m_i elements in the i^{th} shell, $V_i = \frac{3}{m_i}$ corrects the multiplicity, γ_i represents the weight given for each of the neighboring shell with $\sum_{i=1}^3 \gamma_i = 1$ and \vec{u} is a unit vector perpendicular to the plane $(h_1 k_1 l_1)$. To understand the 2D implementation of

Sharp-PFM we will take an example of square lattice and derive its free energy density. For 2D case the free energy potential is derived as follows

$$f(\phi) = \frac{\lambda}{4} \sum_{i=1}^2 \gamma_i \frac{2}{m_i d_i^2} \sum_{k=1}^{m_i} \left\{ \frac{\alpha_i(\vec{r}_i(k))^2 - 1}{\alpha_i(\vec{r}_i(k))^2} \log(1 - \alpha_i(\vec{r}_i(k))^2(2\phi - 1)^2) - (2\phi - 1)^2 \right\} \quad (3.17)$$

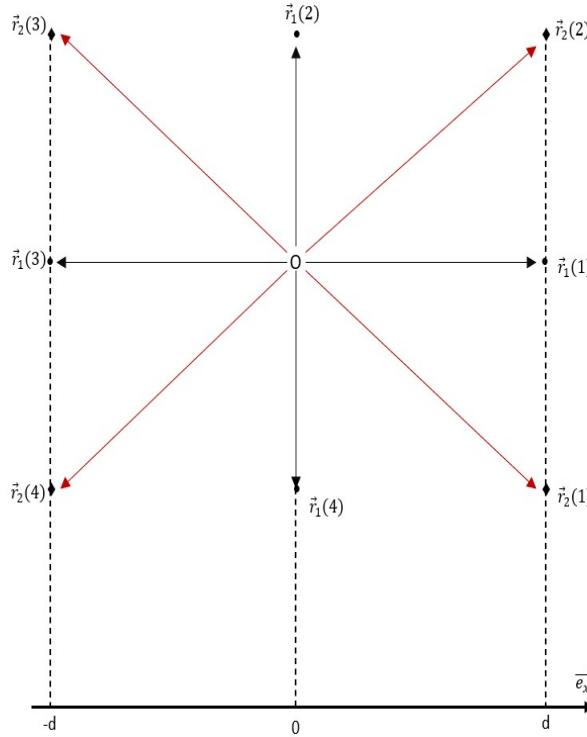


Figure 3.5: A square 2D lattice

As seen from the image Fig. 3.5, in a square lattice for a single point in lattice there are two shells (one represented with black connecting lines and other with red lines) and the direction of \vec{u} is parallel to \vec{e}_x . First shell being the nearest one the values of $\alpha_1[\vec{r}_1(k)]$ are

$$\alpha_1[\vec{r}_1(1)] = \tanh\left(\frac{d}{w}\right) = \alpha$$

$$\alpha_1[\vec{r}_1(2)] = 0$$

$$\alpha_1[\vec{r}_1(3)] = \alpha$$

$$\alpha_1[\vec{r}_1(4)] = 0$$

In second shell the values of $\alpha_2[\vec{r}_2(k)]$ are

$$\alpha_2[\vec{r}_2(1)] = \alpha$$

$$\alpha_2[\vec{r}_2(2)] = \alpha$$

$$\alpha_2[\vec{r}_2(3)] = -\alpha$$

$$\alpha_2[\vec{r}_2(4)] = -\alpha$$

Substituting the different α values along with m_i which is 4 for both shells, $d_1 = d$ and $d_2 = \sqrt{2}d_1$ the final potential equation obtained is

$$f(\phi_n) = \frac{\lambda}{4d^2} \left[\frac{\alpha^2 - 1}{\alpha^2} \log(1 - \alpha^2(2\phi_n - 1)^2) - (2\phi_n - 1)^2 \right] \quad (3.18)$$

Interestingly for the 2D square lattice the potential has turned out to be same as the 1D case. Now using this free energy potential formula in Cahn-Hilliard and Allen-Cahn evolutions the evolution of phases can be performed. The chemical potential is defined in the same way as in Eq. 3.4 with the newly calculated free energy potential substituted.

3.2.3 Cahn Hilliard Evolution

The Cahn-Hilliard evolution equation is

$$\frac{\partial \phi}{\partial t} = \nabla \cdot (M \nabla \mu) \quad (3.19)$$

here

$$\mu = \frac{\delta(F/N_v)}{\delta \phi} = f'(\phi) - \lambda(\nabla^2 \phi) \quad (3.20)$$

$$f'(\phi) = \frac{\lambda}{d^2} \left[\frac{1 - \alpha^2}{1 - \alpha^2(2\phi - 1)^2} - 1 \right] (2\phi - 1) \quad (3.21)$$

3.2.4 Allen Cahn Evolution

$$\begin{aligned} \frac{\partial \phi}{\partial t} &= -L \frac{\delta F}{\delta \phi} \\ \frac{\partial \phi}{\partial t} &= -L \frac{\partial f}{\partial \phi} + \lambda L (\nabla^2 \phi) \end{aligned} \quad (3.22)$$

3.3 Non-Dimensionalisation

The equations and the parameters taken in models are in their non-dimensional form. The dimensional parameters are chosen such that the non-dimensional parameters in our classical phase field models are unity. The characteristic time (t'), length (l') and energy (E') which vary as given in below equation are used to derive the non-dimensional parameters.

$$t' = \frac{l'^2 (c'_p - c'_m)^2}{M'E'} \quad (3.23)$$

$$l' = \left(\frac{K'}{A'} \right)^{1/2} \quad (3.24)$$

$$E' = A' \quad (3.25)$$

The details of non-dimensionalisation, the dimensional values corresponding to non-dimensional parameters used in all simulations are given in Appendix A.

3.4 Numerical Scheme

3.4.1 Classic PFM - Cahn Hilliard

1D Implementation

1D Cahn Hilliard system is solved using semi-implicit Fourier-spectral method by [18]. By using discrete fourier transform (DFT) we go from real space to fourier space and change our equation accordingly. The Cahn Hilliard equation in 1D is Eq. 3.26

$$\frac{\partial c}{\partial t} = M[\nabla^2 \left(\frac{\partial f}{\partial c} \right) - 2K\nabla^4 c] \quad (3.26)$$

c in fourier space can be written as 3.27

$$\tilde{c} = c(k, t) = A \int_{-\infty}^{\infty} c(x, t) \exp(ikx) dx \quad (3.27)$$

This c value in fourier space is substituted in Eq.3.26 and we get the evolution equation in fourier space as given in Eq. 3.29

$$\frac{\tilde{c}^{t+dt} - \tilde{c}^t}{dt} = M[-k^2 \tilde{g}^t - 2k^4 K \tilde{c}^{t+dt}] \quad (3.28)$$

$$\tilde{c}^{t+dt} = \frac{\tilde{c}^t - M k^2 \tilde{g}^t dt}{1 + 2M k^4 K dt} \quad (3.29)$$

here $g = \frac{\partial f}{\partial c}$ and $k = \frac{2\pi}{N}$, N is system size.

2D Implementation

With similar method as in 1D to transform the evolution equation from real space to fourier space we get the 2D Cahn Hilliard evolution equation as 3.31

$$\frac{\tilde{c}^{t+dt} - \tilde{c}^t}{dt} = M[-(k_x^2 + k_y^2) \tilde{g}^t - 2(k_x^2 + k_y^2)^2 K \tilde{c}^{t+dt}] \quad (3.30)$$

$$\tilde{c}^{t+dt} = \frac{\tilde{c}^t - M(k_x^2 + k_y^2) \tilde{g}^t dt}{1 + 2M(k_x^2 + k_y^2)^2 K dt} \quad (3.31)$$

here $k_x = \frac{2\pi}{N_x}$ and $k_y = \frac{2\pi}{N_y}$, where N_x and N_y are system size in two directions.

3.4.2 Classic PFM - Allen Cahn

1D Implementation

In 1D Allen Cahn type evolution we have used both semi-implicit Fourier spectral method and Finite Difference Methods (FDM) techniques. The implementation of spectral method is given in 3.33 and 3.34

$$\frac{\partial \phi}{\partial t} = -L \frac{\partial f}{\partial \phi} + 2KL(\nabla^2 \phi) \quad (3.32)$$

here ϕ is replaced with its reciprocal form as done in previous section. The evolution equations in spectral is given below

$$\frac{\tilde{\phi}^{t+dt} - \tilde{\phi}^t}{dt} = -L\tilde{g}^t + 2Kk^2L\phi^{t+dt} \quad (3.33)$$

$$\tilde{\phi}^{t+dt} = \frac{\tilde{\phi}^t - L\tilde{g}^t dt}{1 + 2Kk^2 L dt} \quad (3.34)$$

In FDM the Allen Cahn evolution equation derived from Eq. 3.32 is

$$\frac{\phi_x^{t+dt} - \phi_x^t}{dt} = -Lg_x^t + 2KL \frac{\phi_{x+dx}^t - 2\phi_x^t + \phi_{x-dx}^t}{dx^2} \quad (3.35)$$

$$\phi_x^{t+dt} = \phi_x^t - Lg_x^t dt + 2KL \frac{\phi_{x+dx}^t - 2\phi_x^t + \phi_{x-dx}^t}{dx^2} \quad (3.36)$$

2D Implementation

In 2D Allen Cahn simulations we used only semi-implicit Fourier spectral. The evolution equation in 2D is

$$\tilde{\phi}^{t+dt} = \frac{\tilde{\phi}^t - L\tilde{g}^t dt}{1 + 2L(k_x^2 + k_y^2)K dt} \quad (3.37)$$

3.4.3 Sharp PFM - Cahn Hilliard

In framing the evolution equations of Sharp-PFM we first derive the free energy potential equation as mentioned in previous sections and then use this as the potential equation normally like it is done in Classic-PFM as mentioned in [4]

1D Implementation

In Sharp-PFM for 1D CH evolution semi-implicit Fourier spectral is used. The evolution equation with semi-implicit Fourier spectral is given in Eq. 3.39. In this equation the free

energy f corresponds to free energy in Sharp-PFM Eq. 3.14 and g is the first derivative of this potential energy.

$$\frac{\partial c}{\partial t} = M[\nabla^2 \left(\frac{\partial f}{\partial c} \right) - \lambda \nabla^4 c] \quad (3.38)$$

$$\tilde{c}^{t+dt} = \frac{\tilde{c}^t - Mk^2 \tilde{g}^t dt}{1 + \lambda k^4 K dt} \quad (3.39)$$

2D Implementation

The 2D Cahn Hilliard evolution equation in Sharp-PFM is 3.40

$$\tilde{c}^{t+dt} = \frac{\tilde{c}^t - M(k_x^2 + k_y^2) \tilde{g}^t dt}{1 + M\lambda(k_x^2 + k_y^2)^2 dt} \quad (3.40)$$

3.4.4 Sharp PFM - Allen Cahn

In Allen Cahn evolution equations for Sharp-PFM both semi-implicit Fourier spectral and Finite Difference Methods (FDM) techniques are used.

1D Implementation

The implementation of spectral method is given in Eq. 3.41 where g is the first derivative of free energy potential which is given by Eq. 3.14

$$\tilde{\phi}^{t+dt} = \frac{\tilde{\phi}^t - L \tilde{g}^t dt}{1 + L\lambda k^2 dt} \quad (3.41)$$

In FDM the evolution equation is given by Eq. 3.43

$$\frac{\phi_x^{t+dt} - \phi_x^t}{dt} = -L g_x^t + L\lambda \left[\frac{\phi_{x+dx}^t - 2\phi_x^t + \phi_{x-dx}^t}{dx^2} \right] \quad (3.42)$$

$$\phi_x^{t+dt} = \phi_x^t - L g_x^t dt + L\lambda \left[\frac{\phi_{x+dx}^t - 2\phi_x^t + \phi_{x-dx}^t}{dx^2} \right] \quad (3.43)$$

2D Implementation

The semi-implicit fourier spectral evolution equation in Sharp-PFM is given by

$$\tilde{\phi}^{t+dt} = \frac{\tilde{\phi}^t - L \tilde{g}^t dt}{1 + L\lambda(k_x^2 + k_y^2) dt} \quad (3.44)$$

The FDM implementation of 2D Sharp-PFM we use is based on the square lattice in Fig. 3.5. After deriving the free energy potential for a given lattice we shall use this

$$\frac{F}{V_0} = \sum_r [f(\phi) + \frac{\lambda}{2} (\nabla_s \phi)^2] \quad (3.45)$$

Here s represents the two shells ($s=2$) around a point as shown in Fig. 3.5. After taking variational derivative we get

$$\mu = f'(\phi) - \lambda \sum_s \nabla_s^2 \phi \quad (3.46)$$

Allen Cahn evolution is

$$\begin{aligned} \frac{\partial \phi}{\partial t} &= -L f'(\phi) + L \lambda (\nabla_1^2 \phi + \nabla_2^2 \phi) \\ \nabla_1^2 \phi &= \frac{2\gamma_1}{4} \sum_{k=1}^4 (\nabla_k^2 \phi) \end{aligned} \quad (3.47)$$

here $\sum_{k=1}^4 \nabla_k^2 \phi$ represents the double derivative about a point across 4 different directions in first shell where x is parallel to \vec{e}_x and y perpendicular to \vec{e}_x . This equation expands to

$$\nabla_1^2 \phi = \gamma_1 [(\phi_{x+dx} - 2\phi_x + \phi_{x-dx}) + (\phi_{y+dy} - 2\phi_y + \phi_{y-dy})] \quad (3.48)$$

Similarly the laplacian across second shell $\sum_{k=1}^4 \nabla_k^2 \phi$ expands to Eq. 3.49. In this equation x is parallel to one of the diagonal (i.e., at 45° to \vec{e}_x) and y is perpendicular to this x. dx and dy correspond to the distance between points in the newly established directions of this shell, which is $\sqrt{2}d$.

$$\nabla_2^2 \phi = \gamma_2 [(\phi_{x+dx} - 2\phi_x + \phi_{x-dx}) + (\phi_{y+dy} - 2\phi_y + \phi_{y-dy})] \quad (3.49)$$

Finally the FDM equation for 2D Sharp-PFM is given in Eq. 3.50.

$$\phi_x^{t+dt} = \phi_x^t - L g_x^t dt + L \lambda [\nabla_1^2 \phi + \nabla_2^2 \phi] \quad (3.50)$$

3.5 Interfacial Energy Calculation

For a free energy functional of the form 3.1 the interfacial energy is numerically calculated as sum of potential and gradient energy of order parameter at all points from which the total energy (potential + gradient) of phases with equilibrium order parameter (bulk phase) is removed. This gives the energy of non-equilibrium order parameter values which constitute interfacial energy.

In Sharp Phase Field Model as the potential of equilibrium order parameters values is negative, all the values are added with the magnitude of height of potential energy curve

to make the potential of bulk phases zero.

In 1D, the interfacial energy σ is 3.51 and the energy of bulk phases is zero.

$$\sigma = \sum_{x=0}^n [f(c)_x + K(\nabla c)_x^2] dx \quad (3.51)$$

In 2D the interfacial energy is 3.52

$$\sigma = \sum_{x=0}^n [\sum_{y=0}^n [f(c)_{(x,y)} + K(\nabla c)_{(x,y)}^2]] dx^2 \quad (3.52)$$

Chapter 4

Results and Discussion

4.1 Grid Pinning

4.1.1 Classic PFM

To visualise Grid Pinning we take a 1D system with two equilibrium order parameter values separated by an interface. This can be effectively represented with Eq.3.5. Now a driving force is introduced in the form of interpolation function $p(\phi) = u(3\phi^2 - 2\phi^3)$ in the free energy functional equation. The interpolation function increases the energy of phase 1 favouring growth of phase 0 and parameter 'u' in $p(\phi)$ decides the magnitude of driving force.

This free energy functional with a certain driving force is now evolved using Eq. 3.1,3.2,3.3,3.9 and Finite Difference Method. Taking the model parameters $A = 1; K = 1; L = 1$ with different grid spacing. During the evolution the interface energy and position, where $\phi = 0.5$ is tracked with respect to time. As seen in Fig. 1.1 for a system with higher grid spacing the evolution stops after certain time or slows down whereas these effects are not seen in systems with grid spacing less than 1. This effect is readily visible in system where the grid spacing is less than or equal to the smallest feature in system which is interface here and its analytical width is equal to 4 [7].

There is another indicator for Grid Pinning which is the variation of interface energy as it moves, as shown in Table 4.1. The amplitude of variation in interface energy as it is moving is higher for systems which are prone to grid pinning, that are with higher grid spacing.

Δx	Interface Energy	Amplitude
0.5	0.3327	9.4×10^{-6}
1	0.3305	1.6×10^{-4}
2	0.3203	0.011
4	0.2304	0.07

Table 4.1: Average interface energy and amplitude of variation of interface energy during motion of interface in Classical-PFM for a Δx

4.1.2 Sharp Phase Field Method

In Sharp-PF model we again follow a similar method as in Classic-PFM to visualise grid pinning. Taking a system which has an interface separating the equilibrium values based on Eq.3.12. A driving force is introduced just as in previous case and the system is let to evolve using Allen Cahn evolution. The system parameters taken here are $\lambda = 1$; $d/w = 2$ and different grid spacing values. The variation of interface energy during interface motion is shown in Table 4.2 and the interface motion is shown in Fig. 4.1.

Δx	Interface Energy	Amplitude
1	0.4426	8.9×10^{-9}
2	0.2213	3.8×10^{-8}
4	0.1106	7.5×10^{-8}

Table 4.2: Average interface energy and amplitude of variation of interface energy during motion of interface in Sharp-PFM for a Δx

As seen from the Fig. 4.1 even in a system with very large grid spacing as $\Delta x=4$ the interface is moving without slowing down. Also, the variation in interface energy is very small indicating that grid pinning effect is not present in system at higher grid spacing.

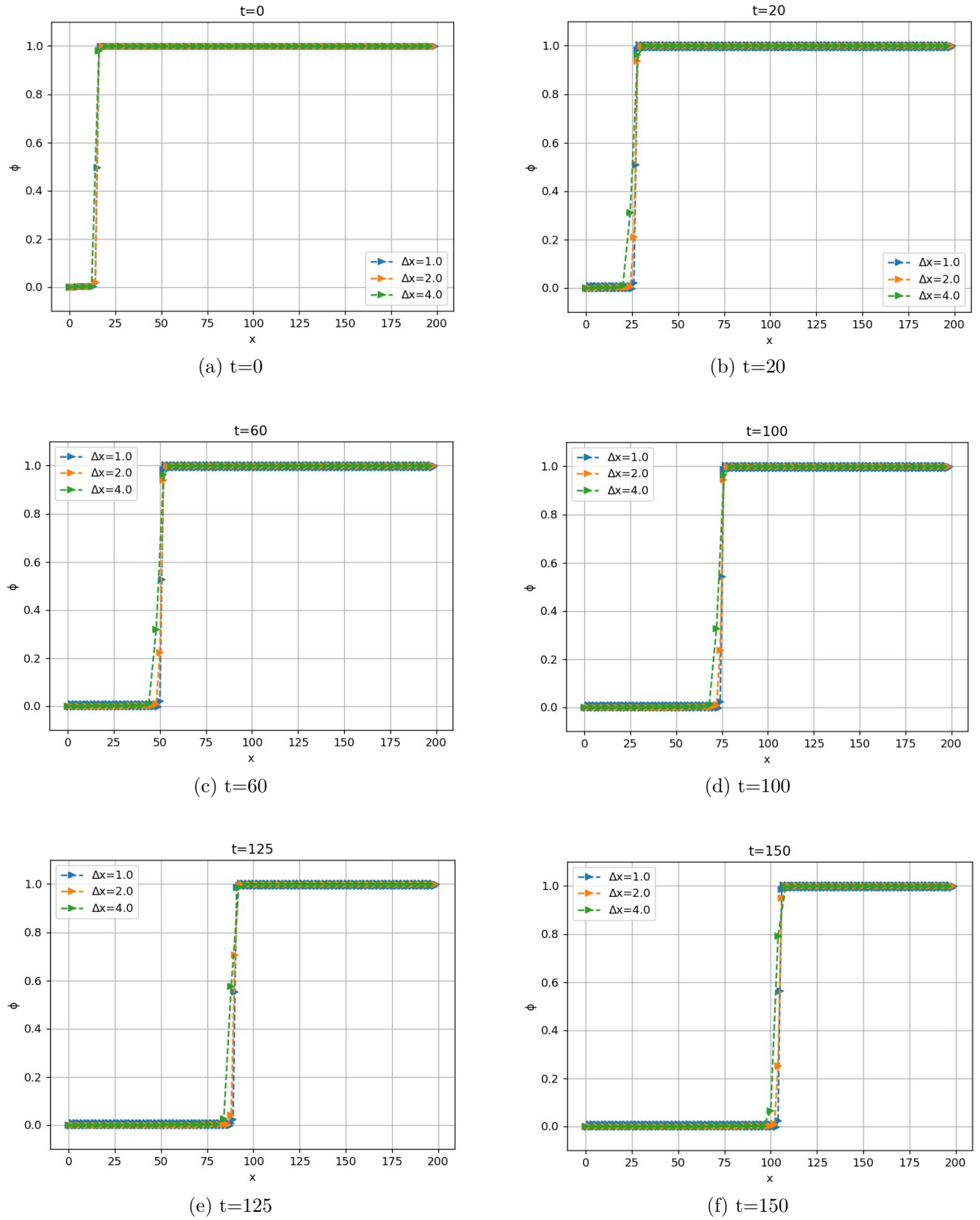


Figure 4.1: 1D interface motion in Sharp-PFM

4.2 Matching Interfacial Energy

In Classic-PFM with $A = K = 1$, the analytical interface energy is $1/3$ and interfacial width is 4 [7] which can be obtained using a smaller grid spacing Δx as shown in Table 4.3.

Δx	Interface Energy	Interface Width
1.0	0.3306	4.3286
0.5	0.3326	4.0833
0.25	0.3332	4.0211
0.1	0.3333	4.0037

Table 4.3: Interface Energy and width variation with grid spacing in PFM

In Sharp-PFM with $d/w = 2$ the interface energy is $0.4426\frac{\lambda}{d}$ and with $d/w = 1$ the interface energy is $0.2945\frac{\lambda}{d}$. In Sharp-PFM with changing 'w' parameter the diffuseness

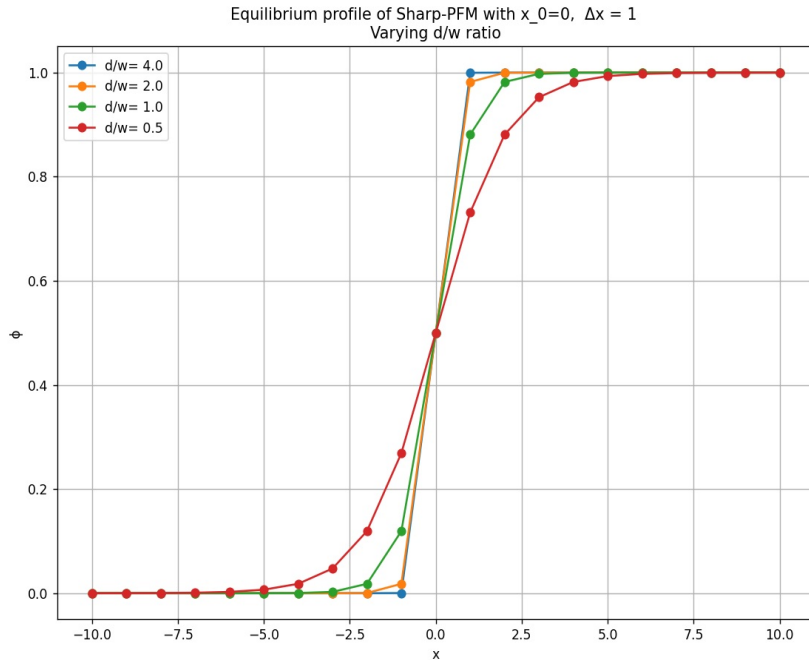


Figure 4.2: Equilibrium Profile of Sharp-PFM

and number of points of interface in the equilibrium profile can be changed. As seen in Fig. 4.2 with decreasing w (with same grid spacing, d) the equilibrium profile interface is becoming sharper and model with $d/w = 2$ has lesser number of points than in $d/w = 1$.

To match the interfacial energy across different models the numerically calculated interface energy in Sharp-PFM and analytical interfacial energy of Classical-PFM. For grid spacing of 1 and models $d/w = 1$ and $d/w = 2$ the calculated λ values are 1.1319 and 0.7531. With these changed λ values the numerical interface energy calculated (in 1D) as shown in Table 4.4 and they are used in further simulations to compare the Sharp-PF models with Classic-PF models.

λ	d/w	Interface Energy
1.1319	1	0.3333
0.7531	2	0.3334

Table 4.4: Interface Energy for a given and d/w in Sharp-PFM matching with PFM

4.2.1 Ponderation Coefficients

In 2D Sharp-PF model Eq. 3.15 the term γ_i is called as ponderation coefficient which gives a particular weight for each shell (Fig. 3.5). To find these values we consider a 2D square lattice system in which there is one single interface perpendicular to x-direction (e_x or [10]). In another system we take the interface to be perpendicular to the diagonal direction [11]. Now by assuming some initial γ values, the interface in each model is let to evolve with AC evolution by fixing the boundary values ,with zero slope, for some time. During the evolution the interface energy is tracked w.r.t. time and an average interface energy is computed.

A parameter $R = \sigma_{[10]} - \sigma_{[11]}$ is taken which is minimised, until R goes below a certain threshold very close to 0, using bisection method with some assumed starting values of γ . The ponderation coefficient values that we get this minimisation method are the required values.

For the Sharp-PF models given in Table 4.5 the calculated γ values are 0.757 and 0.662 for models with d/w values of 1 and 2 respectively.

4.3 Allen Cahn Comparison

In this section we compare the Classical and Sharp Phase Field methods by employing them in two different problems. One is in one-dimension where interface motion behaviour is studied followed by comparison in two-dimension where the kinetics of curved boundary motion is studied.

4.3.1 1D Comparison

In a 1D system starting with an equilibrium interface in both Classic-PFM and Sharp-PFM, based on Eq. 3.5 and 3.12 respectively, a driving force is introduced in the form of interpolation function $p(\phi) = u(3\phi^2 - 2\phi^3)$ in the free energy functional equation. The interpolation function increases the energy of phase 1 favouring growth of phase 0 and parameter 'u' in $p(\phi)$ decides the magnitude of driving force.

Four models, two in Classic-PFM and two in Sharp-PFM are taken with same driving force and interface mobility in all cases. The interfacial energy is matched across all cases, as shown in table Table 4.5. As the interface moves growing the phase 0 the interface

position where $\phi = 0.5$ is tracked with time. From the data of interface position and time the velocity of interface motion in a model is calculated.

PFM	PFM	S-PFM	S-PFM
A=K=1; L=1; $\Delta x = 1$	A=K=1; L=1; $\Delta x = 0.5$	$\lambda = 1.1319$ d/w=1; L=1; Δx (or d)=1	$\lambda = 0.7531$ d/w=2; L=1; Δx (or d)=1

Table 4.5: Parameters for Allen Cahn Evolution in 1D

The velocity of interface is proportional to the driving force where mobility is the proportionality constant [19]. From the equation $V = M.F$ we calculate the mobility values for every model. The mobility values calculated are as shown in Table 4.6

PFM ($\Delta x=0.5$)	PFM ($\Delta x=1$)	S-PFM (d/w=1)	S-PFM (d/w=2)
5.96	5.84	3	1.5

Table 4.6: Mobility Values from 1D Allen-Cahn simulations

Across all the models the interface energy is matched and also the driving force provided is same, but the velocity of interface motion is different in each model. Sharp-PFM moved with a slower velocity. So the interface mobility parameter(L) which is taken to be same across all the models can be changed to match the velocity across models. Taking L of a Sharp-PFM to be the ratio of mobility of classic-PFM with the respective model gives the new mobility values of the Sharp-PFM as $L \approx 2$ and $L \approx 4$ for model with d/w=1 and d/w=2 respectively.

Now, by performing another simulation in Sharp-PFM with these changed L values the interface velocity calculated is same as the Classic-PFM. This indicates that a Sharp-PFM can faithfully represent a Classical-PFM by changing the parameters as required.

4.3.2 2D Curved Grain Motion

For the motion of a curved boundary there is an analytical relation describing the velocity variation with time [11]. We perform simulation with similar setup in different models to compare our numerical results with the analytical one. For this in a 2D system with a size of 256 x 256, a circular grain with order parameter as 1, is introduced in another grain having order parameter as 0. Now the system is let to evolve using Allen-Cahn evolution using semi-implicit Fourier spectral method [18] and solved using FFTW3 package [20]. The simulation is performed until the circular grain dissolves, which is due to higher interface energy because of curvature of grain. This simulation is performed across all four models with parameters as shown in Table 4.5. During the evolution the total energy

in system and the area fraction of phase 1 is calculated by considering all points with $\phi \geq 0.5$ as one phase and the rest as another. Also, the radius across 4 different directions, horizontal, vertical and two diagonals, were calculated with respect to time to check for circularity during the evolution. The values of ponderation coefficients used in Sharp-PFM are calculated as, for $d/w=1$ $\gamma_1 = 0.757$ and for $d/w=2$ $\gamma_1 = 0.662$.

To calculate the mobility values in two dimensional case we take slope of $Radius^2$ vs time to calculate velocity as in Eq.4.1. The driving force is shown in 4.2 and mobility values obtained from the 2D simulations are given in Table 4.7. The mobility values we got are approximately same as the values from 1D simulations, except for Classic-PFM with $\Delta x=1$ having a slightly higher increase in mobility value.

$$Velocity = \frac{dr}{dt} = \frac{d(r^2)}{dt} \frac{1}{2r} \quad (4.1)$$

$$Driving Force = \sigma \cdot \kappa = \frac{\sigma}{r} \quad (4.2)$$

PFM ($\Delta x=0.5$)	PFM ($\Delta x=1$)	S-PFM ($d/w=1$)	S-PFM ($d/w=2$)
6	6	2.98	1.81

Table 4.7: Mobility Values from 2D simulations

The scaled interfacial mobility (L) values for 2D Allen Cahn models of S-PFM are calculated just like in 1D case to match the velocity. The new L values are 2 for model with $d/w=1$ and 3.3 for model with $d/w=2$. Using these changed interface mobility values for Sharp-PFM another simulation is performed in both the Sharp-PF models. During the evolution the total energy in system and the area fraction of phase 1 is calculated tracked with respect to time.

As shown in Fig. 4.3 the microstructural evolution of Classical-PFM ($\Delta x = 0.5$) and Sharp-PFM ($d/w=1$) is compared where it can be seen that the microstructure at a given time step is very similar across models. Also it can be seen in Fig. 4.3 that the interface is more diffuse in Classical-PFM compared to Sharp-PFM.

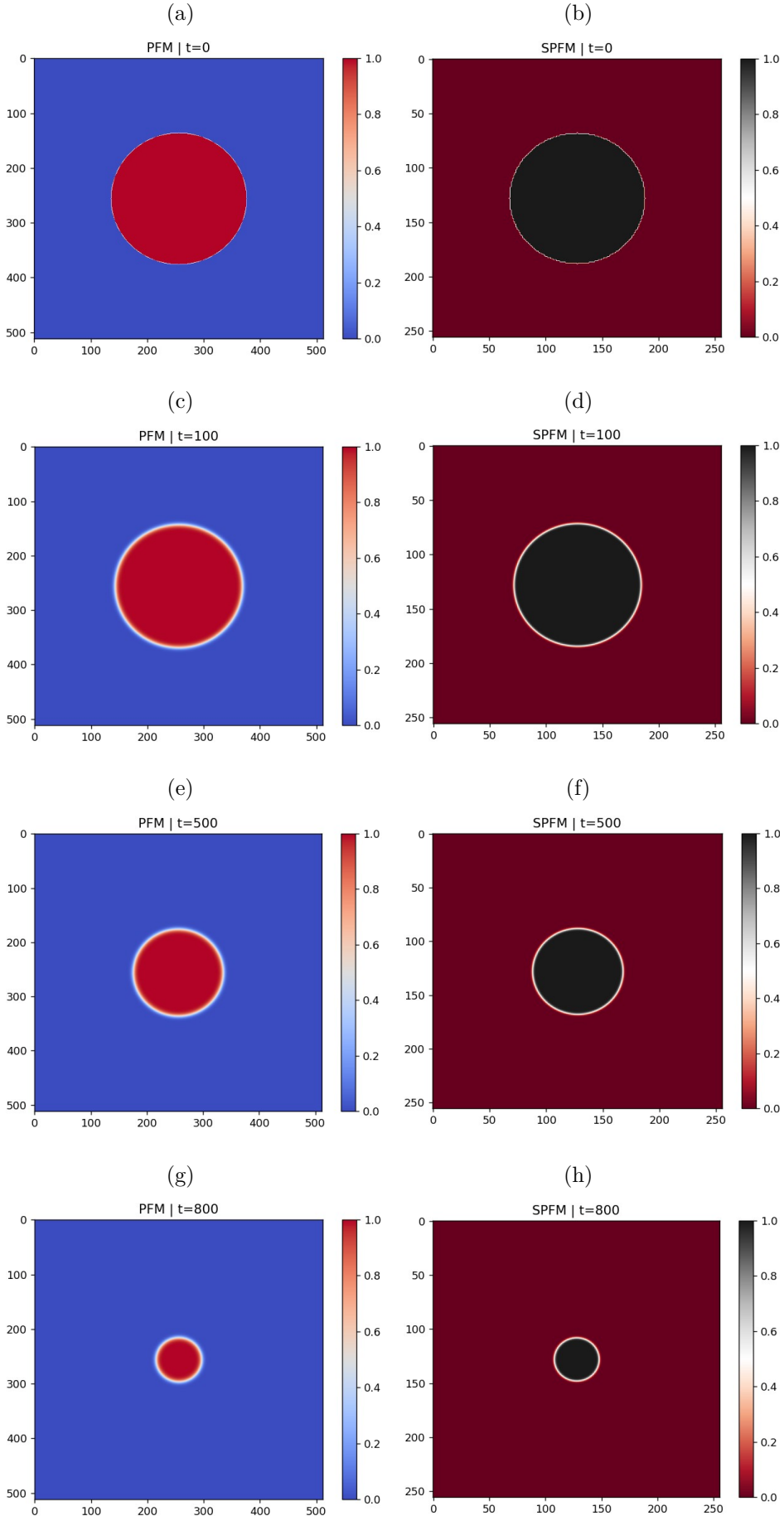


Figure 4.3: Microstructural evolution in Allen Cahn evolution for Classical-PFM, with $\Delta x = 0.5$, and Sharp-PFM, $d/w=1$, at different time steps.

From the radius calculated in 4 different directions in each model it is found that the all the radius values in a model are very close to each other at every time step. So it can be inferred that the circularity is present at every time step in each of the models.

The kinetics of motion of a curved boundary depends on the number of points in the interface [14]. For a curved boundary the analytical relation of velocity of boundary is given in Eq.4.3 [11].

$$\text{Velocity} = \frac{-2LK}{R} \quad (4.3)$$

Using the relation Velocity = dR/dt we get the analytical relationship of radius (R) with model parameters as 4.4

$$R^2 = R_0^2 - 4LKT \quad (4.4)$$

The results of numerical simulations comparing with the analytical relation is shown in Fig. 4.4a and an enlarged portion in Fig. 4.4b. As it can be seen from the Fig. 4.4b the Sharp-PFM with d/w = 1 and Classic-PFM with dx=0.5 are indistinguishable from the analytical profile.

The error percentage between the slope of R^2 vs time results from different models and analytical result Eq.4.4 is given in Table 4.8. Even in Sharp-PFM it seen that an interface having higher number of points has better kinetic accuracy just like in Classical-PFM [14].

PFM ($\Delta x=0.5$)	PFM ($\Delta x=1$)	S-PFM ($d/w=1$)	S-PFM ($d/w=2$)
0.06	1.48	0.06	1.72

Table 4.8: Error percentage between slope of R^2 vs time profile of a numerical model and analytical slope

CPU and simulation time is compared for the two models with the best accuracy. Although the number of grid points in Classical-PFM ($\Delta x = 0.5$) is 4 times higher than Sharp-PFM ($d/w=1$; $d/\Delta x = 1$), the computation time (CPU time) required per grid point per time step in simulation for Classical-PFM was lower, 5×10^{-8} s, than that of Sharp-PFM, 10×10^{-8} s. It is because in Sharp-PFM there are more calculations in the interface energy equation and also the evolution equation. The maximum Δt that was required to achieve the reported level of accuracy was 10^{-2} in Classical-PFM and 10^{-1} in Sharp-PFM. Considering all these factors the simulation time in Sharp-PFM was 20 times higher than that of Classical-PFM representing same system with similar same kinetics.

So a Sharp-PF model can faithfully represent a Classical-PF model with smaller number of grid points and also has faster simulation time in Allen-Cahn evolution models.

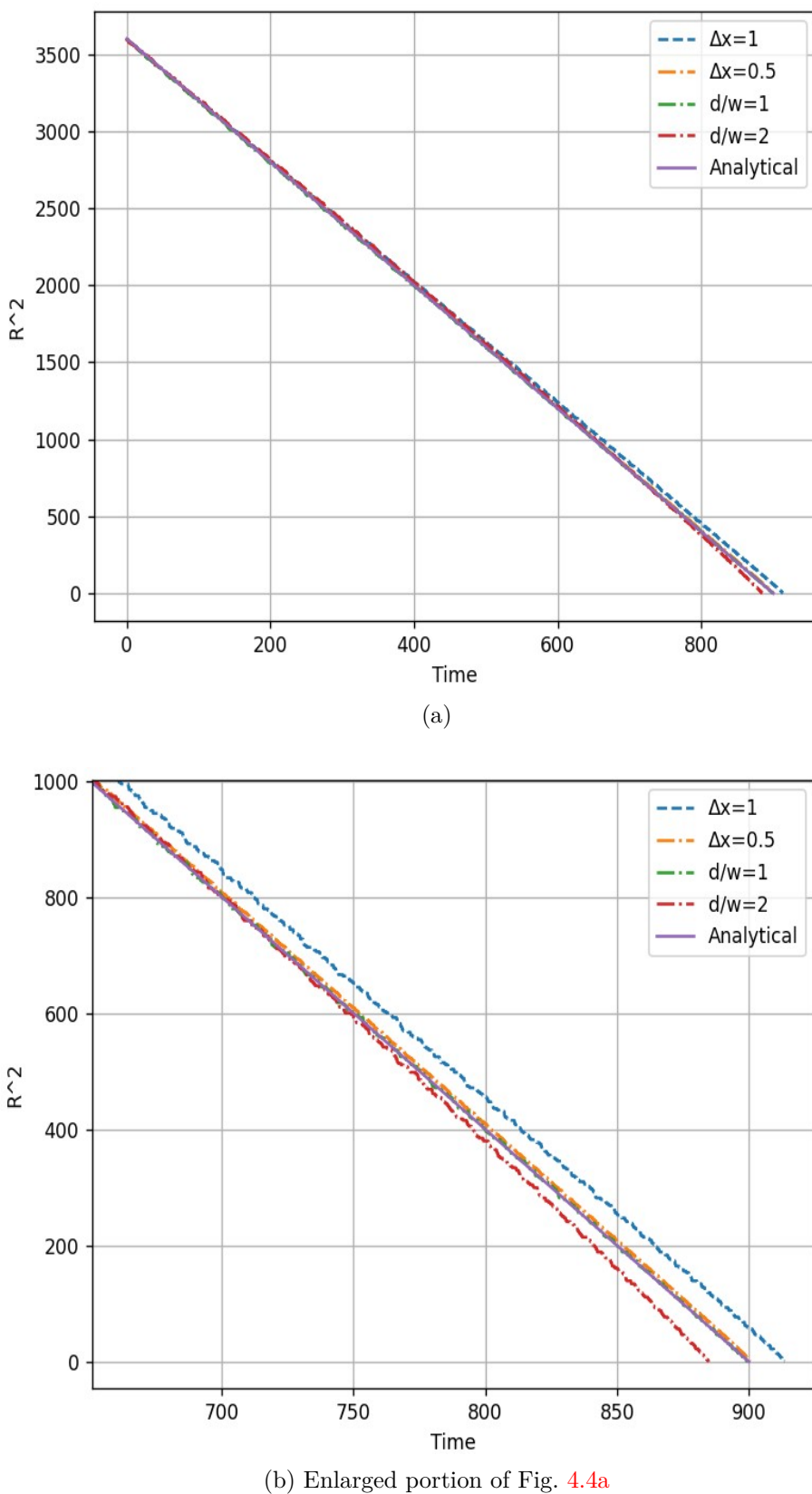


Figure 4.4: Comparison of R^2 vs time in Allen-Cahn evolution across different models

4.4 Cahn Hilliard Comparison

The Classical and Sharp phase field models are compared in Cahn-Hilliard evolution equation using three different problems. First is early stage decomposition where the maximally growing wavelength is analysed, followed by a 1D Growth comparison by considering composition dependent diffusivity. Finally 2D Coarsening simulations are performed in both the models.

4.4.1 Early Stage Spinodal Decomposition

During spinodal decomposition there exists a critical wavelength [10] above which a disturbance in the unstable region grows into different phases having equilibrium composition values. This can be checked with finding the maximally growing wavelength occurring during simulations. During evolution the number of transitions across $\phi = 0.5$ were tracked. The ratio of number points in system with half the number of transitions gives average wavelength in system at that particular time. Also, the wavelength distribution in the system at a particular time is calculated.

This simulation is performed only on two models now, one each from Classic-PFM and Sharp-PFM. The model parameters used in these simulations is given in Table 4.9. The interfacial energy is matched across both the models as done previously.

PFM	S-PFM
A=1; K = 1; M=1; Δx=1	$\lambda = 1.1319$; $d/w = 1$; $M = 1$; $d = 1$

Table 4.9: Model parameters in 1D Spinodal Decomposition Simulation

For the evolution we used semi-implicit Fourier spectral method and solved using FFTW3 package [20]. The wavelength calculated during simulation in two models are shown in Fig. 4.5 and Fig. 4.7. Theoretically the critical wavelength above which a disturbance in system grows, or splits into equilibrium values, is given by Eq. 4.5 and the maximally growing wavelength is $\sqrt{2}\lambda_{critical}$ [10].

$$\lambda_{critical} = \left[\frac{-8\pi^2 K}{\frac{\partial^2 f}{\partial c^2}} \right]^{1/2} \quad (4.5)$$

For the Classic-PFM the analytical maximally growing wavelength is 4π and for the Sharp-PFM it is 8.25. As seen from Fig. 4.5 and Fig. 4.7 there is a time period in the beginning where the wavelength is almost constant for some time, those values are around 13 for Classic-PFM and 8.5 for Sharp-PFM. From Fig. 4.6 we can see that for Classic-PFM at time 50 the most number of wavelengths present in system are at around 12.5 indicating that the maximally growing wavelength in system is also in this range.

Similarly from Fig. 4.8 for Sharp-PFM at time 20 there are more number of wavelengths present around 8.5 indicating that maximally growing wavelengths in this system is also around 8.5 as also seen in Fig. 4.7.

From Fig. 4.9 and Fig. 4.10 we can see that in Sharp-PFM the equilibrium values are reached much earlier compared to Classic-PFM. This is expected as the critical wavelength in Sharp-PFM is less, so the atoms has to travel a shorter distance to reach the equilibrium values and it can happen with a smaller $\lambda_{critical}$.

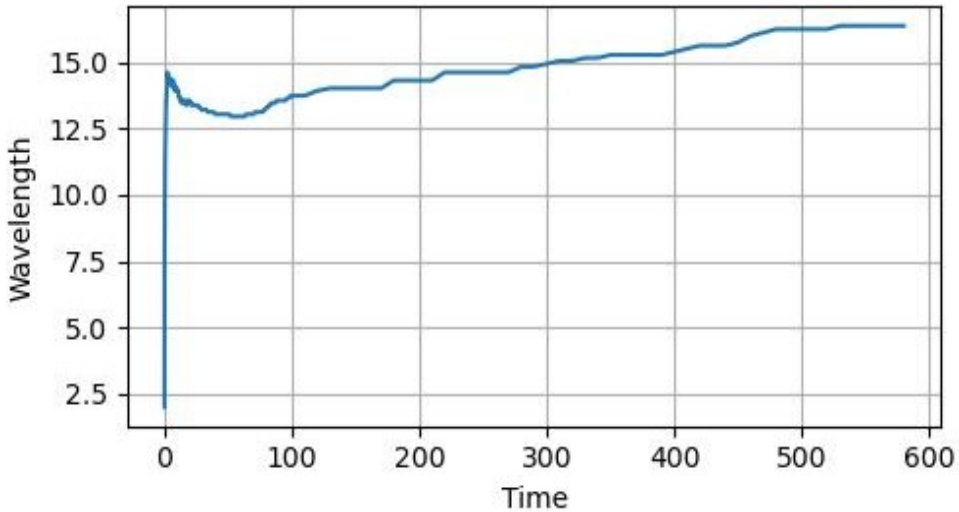


Figure 4.5: Variation of wavelength with time in Classical-PFM

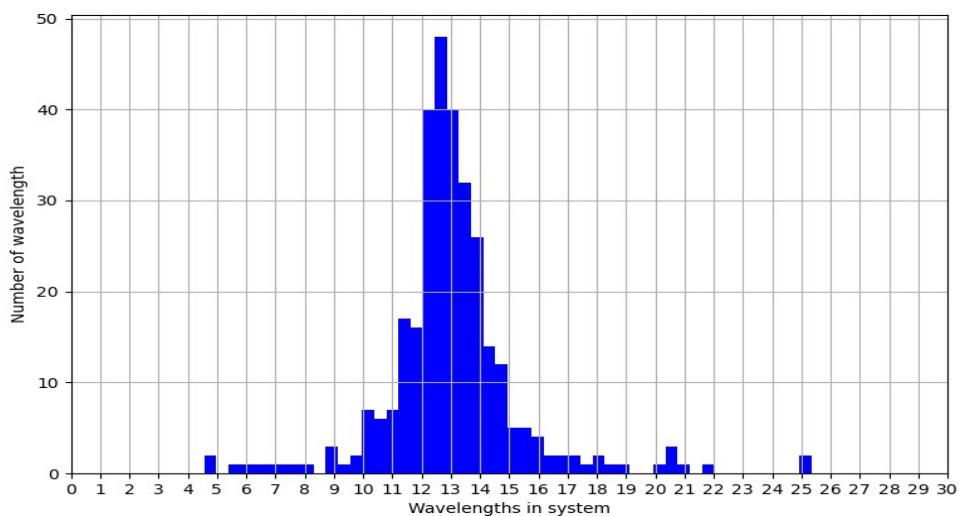


Figure 4.6: Wavelength Distribution in Classical-PFM at time 50

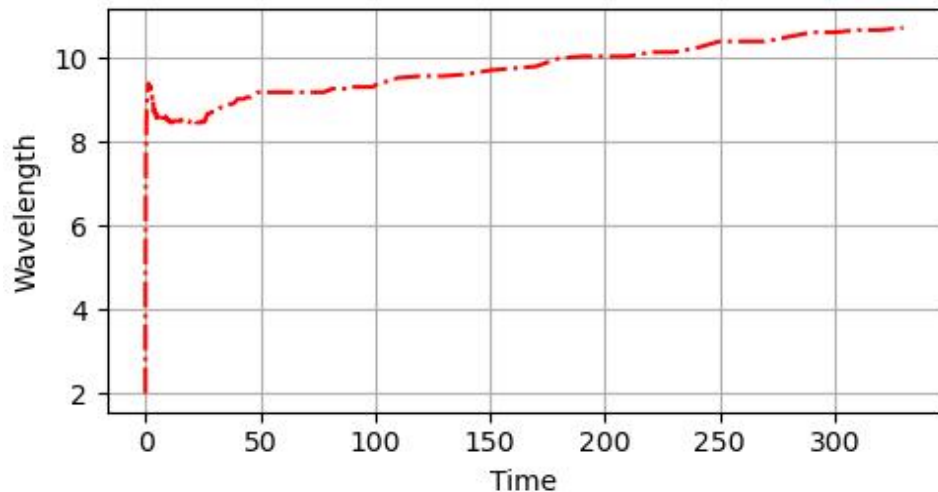


Figure 4.7: Variation of wavelength with time in Sharp-PFM

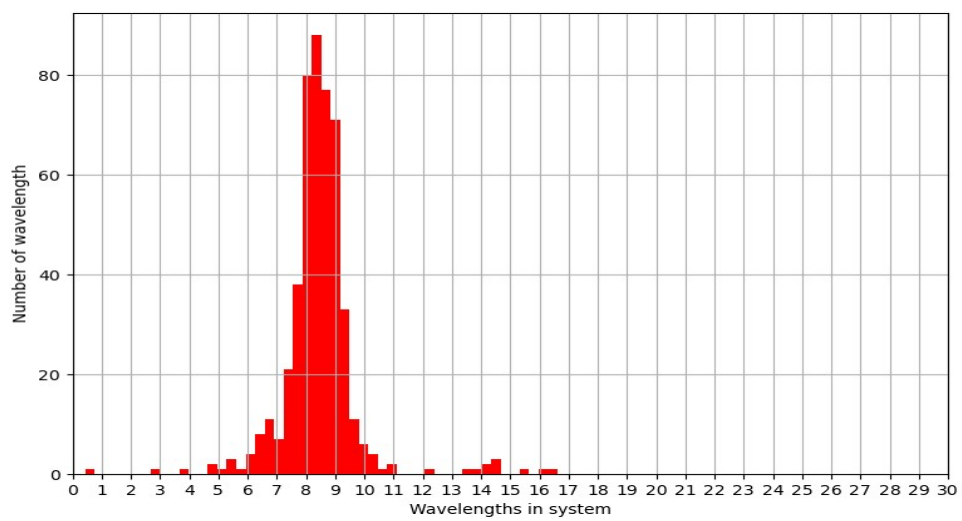


Figure 4.8: Wavelength Distribution in Sharp-PFM at time 20

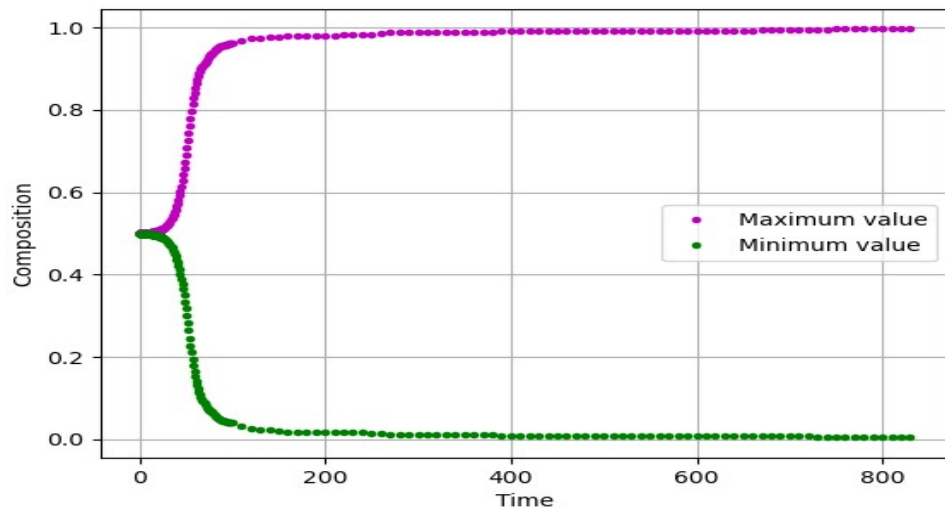


Figure 4.9: Variation of order parameter values with time in Classical-PFM

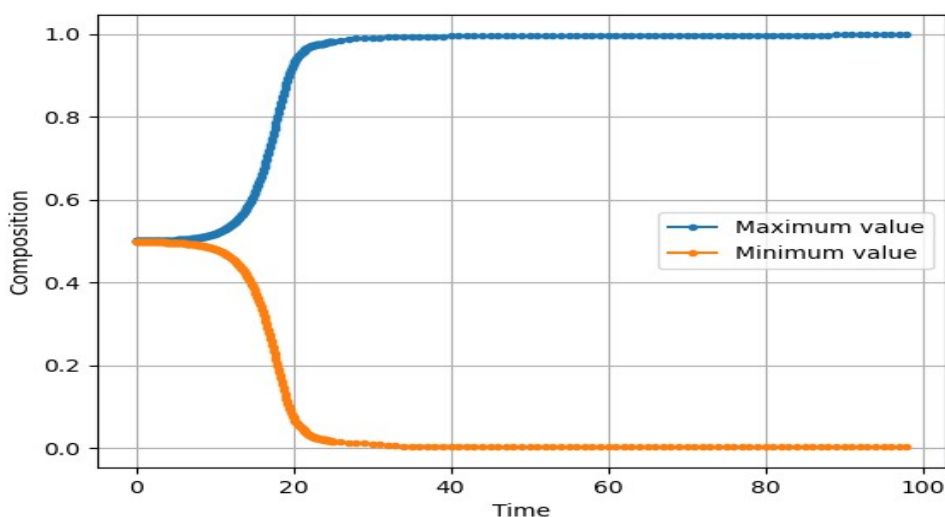


Figure 4.10: Variation of order parameter values with time in Sharp-PFM

4.4.2 1D Growth

To understand the growth of a precipitate due to the effect of only diffusivity, a 1D simulations gives better results as in 2D, interface curvature effects come into picture. We are comparing the effect of composition variation on diffusivity in both Classic and Sharp PF models. In Cahn Hilliard models the diffusivity is product of atomic mobility parameter, M in model, and double derivative of free energy (Eq. 4.6) [21].

In the Sharp-PFM with values given in Table 4.9 the plot of $\frac{\partial^2 f}{\partial c^2}$ is as shown in Fig. 4.12 and the variation in Classic-PFM is shown in Fig. 4.11. In Sharp-PFM the inflection point is at $c=0.16$ and in Classic-PFM it is at $c=0.21$. The variation of $\frac{\partial^2 f}{\partial c^2}$ in Sharp-PFM is much higher so there will be pronounced effect of compositional variation on Diffusivity.

$$D = M \left(\frac{\partial^2 f}{\partial c^2} \right) \quad (4.6)$$

In a 1D system which is supersaturated, a small precipitate is introduced at the center and is let to evolve with Cahn Hilliard evolution. For the evolution we used semi-implicit Fourier spectral method and solved using FFTW3 package [20]. During evolution, the size of precipitate is calculated as distance from center of precipitate to where c is 0.5. From the relation of $S^2 - S_0^2 = \alpha^2 t$ we calculate the growth parameter α from our simulations.

In a system of size 2×10^4 a small precipitate of size 20 grid points is introduced. With the same parameters as given in Table 4.9 we let the system evolve using Cahn Hilliard model with periodic boundary conditions. The precipitate has the composition of 1 and the composition of matrix is same as the volume fraction of precipitate [13]. The simulation is performed for two volume fractions, 0.1 and 0.15, in both Classical and Sharp phase field methods. When the far-field composition c_∞ decreases i.e., the diffusion fields from adjacent precipitates overlap the evolution is stopped as it is end of growth stage. From the plot of $S^2 - S_0^2$ vs time we take the slope just before end of simulation as square of growth parameter. As given in paper [21] we calculated the variation of theoretical growth parameter with respect to far-field composition and also the growth parameter we obtained from our simulations.

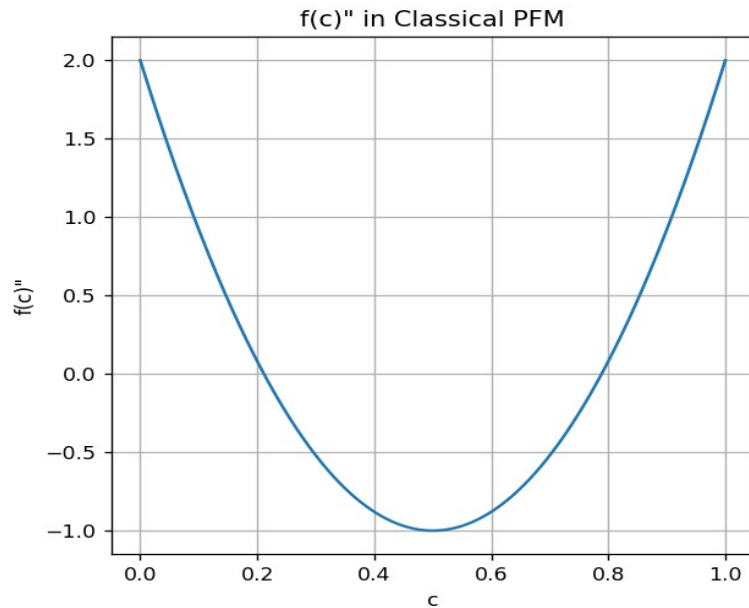


Figure 4.11: Variation of $\frac{\partial^2 f}{\partial c^2}$ with composition in Classical-PFM

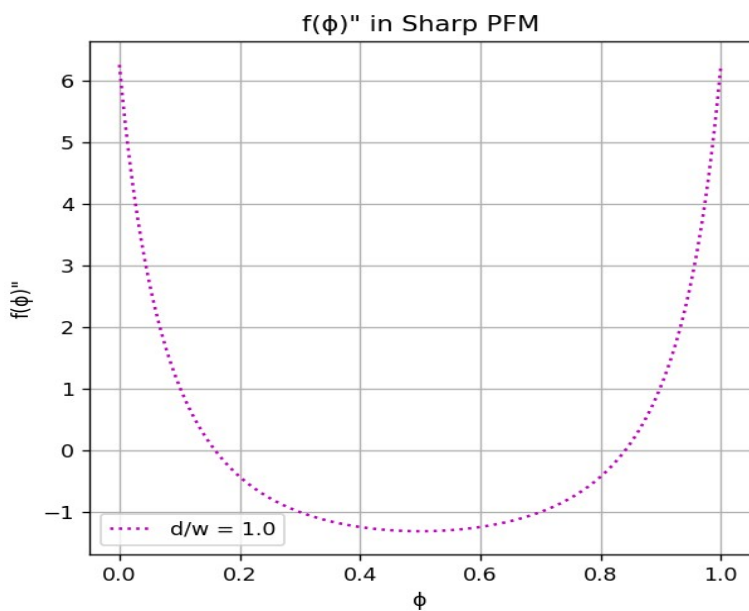


Figure 4.12: Variation of $\frac{\partial^2 f}{\partial \phi^2}$ with ϕ in Sharp-PFM

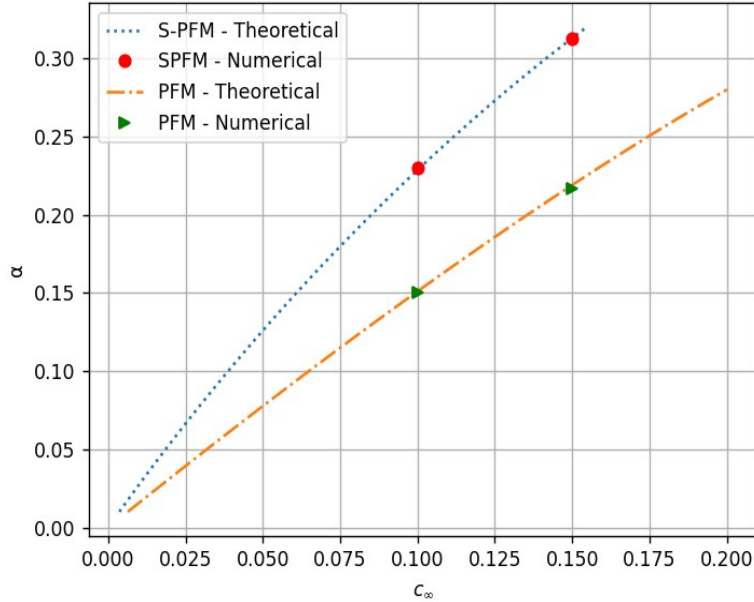


Figure 4.13: Theoretical and numerical growth rates in PFM and S-PFM

As shown in Fig. 4.13 the growth rates obtained from both the models are equal to theoretical predictions. In Fig. 4.13 the dotted lines indicate the theoretical values of growth rates. For a given c_∞ or volume fraction of precipitate the growth rate is much higher in Sharp-PFM compared to Classic-PFM even for equal atomic mobility parameter M. This is because of the high values of $\frac{\partial^2 f}{\partial c^2}$ in Sharp-PFM as shown in Fig. 4.12. The values of growth rates for different volume fractions in both the models is given in Table 4.10. As atomic mobility parameter (M) is same across models, M in Sharp-PFM should be scaled accordingly to get similar growth rate as that of Classical-PFM.

c_∞	PFM	S-PFM
0.1	0.15	0.23
0.15	0.22	0.31

Table 4.10: Growth rates for Classical and Sharp PF models for different c_∞

4.4.3 2D Coarsening

Coarsening is a problem which can be studied purely using Cahn-Hilliard evolution so a better comparison of Classical-PFM and Sharp-PFM can be made. A 2D supersaturated system is evolved using Cahn-Hilliard evolution and the coarsening behaviour is studied in both the models and compared with each other.

A system of size 1024×1024 is taken with precipitates having radius slightly higher than the critical radius. These precipitates are introduced at a minimum distance from each other using pseudo-random number function generator. For a given volume fraction (V_f) half of it is included in precipitate and other half in matrix. This system is now evolved with Cahn Hilliard evolution equation using periodic boundary conditions. During evolution the average radius and number density of particles is calculated using Hoshen-Kopelman algorithm [22]. Also, the volume fraction of precipitate is tracked with time by considering everything above $c=0.5$ as precipitate and rest as matrix. These simulations were performed 3 times with different seed each time for random number generator for a given volume fraction. The final results for a given volume fraction is taken as the average of the three simulations. This simulation is performed for 3 different volume fractions, 0.15, 0.2, 0.25, in both Classic-PFM and Sharp-PFM. The parameters of the model are given in Table 4.9 and each simulation is evolved till time of 10^5 . The critical radius was calculated using Eq 4.7 [23].

$$r^* = \frac{\sigma}{-\Delta G_v} \quad (4.7)$$

where

$$\Delta G_v(c_\infty) = -[f_{c_\infty} + (1 - c_\infty) \left(\frac{\partial f}{\partial c} \right) \Big|_{c=c_\infty}] \quad (4.8)$$

From the coarsening microstructures of both the models, as shown in Fig. 4.14, it is seen that coarsening of precipitates is happening. Smaller precipitates are getting dissolved while larger precipitates are growing.

The volume fraction calculated is shown in Fig. 4.15. The volume fraction is seen to be increasing and becoming almost constant in both the models for all cases, indicating the coarsening regime where volume fraction remains constant. It can be seen in Fig. 4.15 that in Sharp-PFM the coarsening regime is reached at an earlier time in accordance with our 1D Growth simulation results.

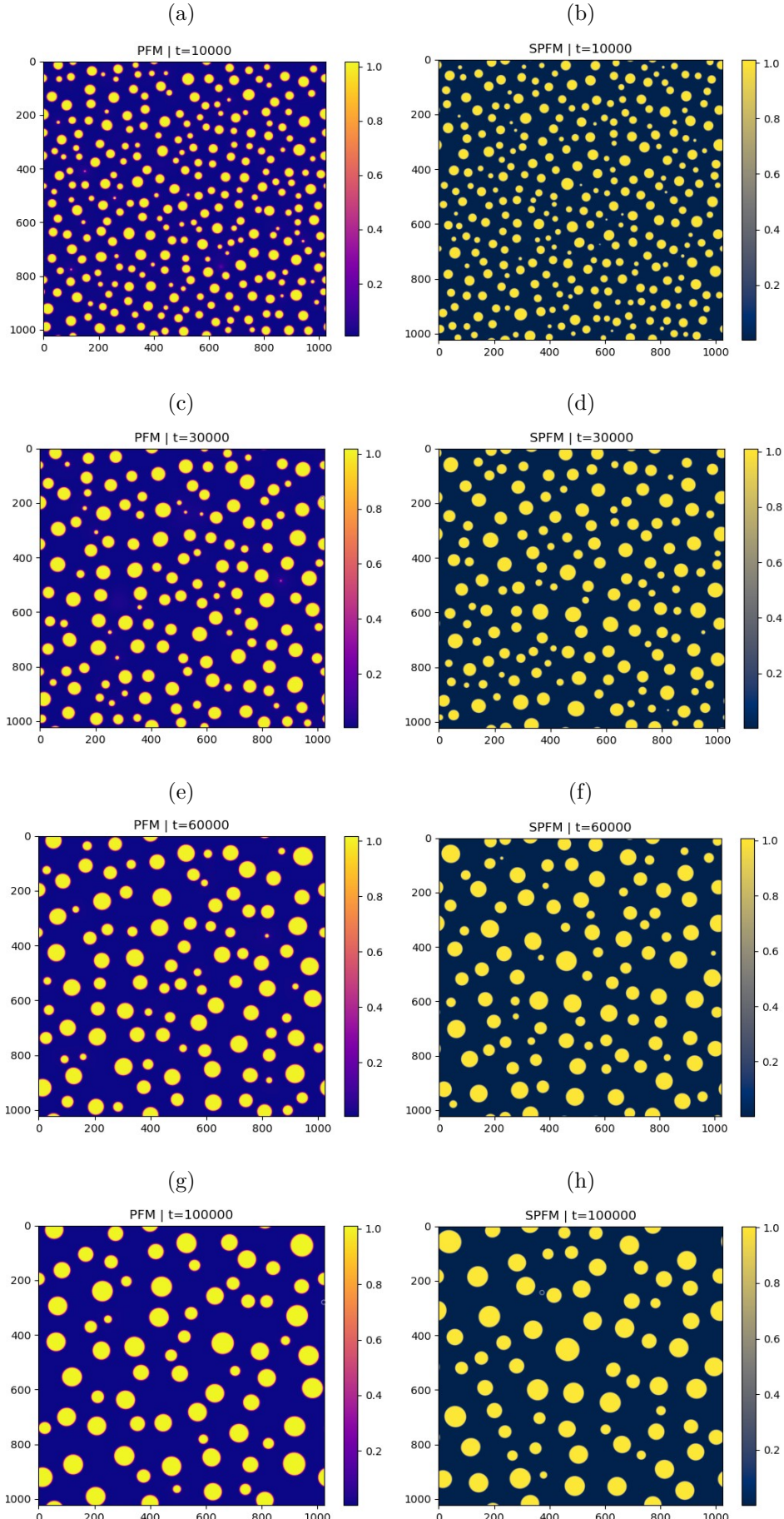


Figure 4.14: Microstructural evolution during coarsening for V_f of 0.2 in Classical-PFM and Sharp-PFM at different time steps.

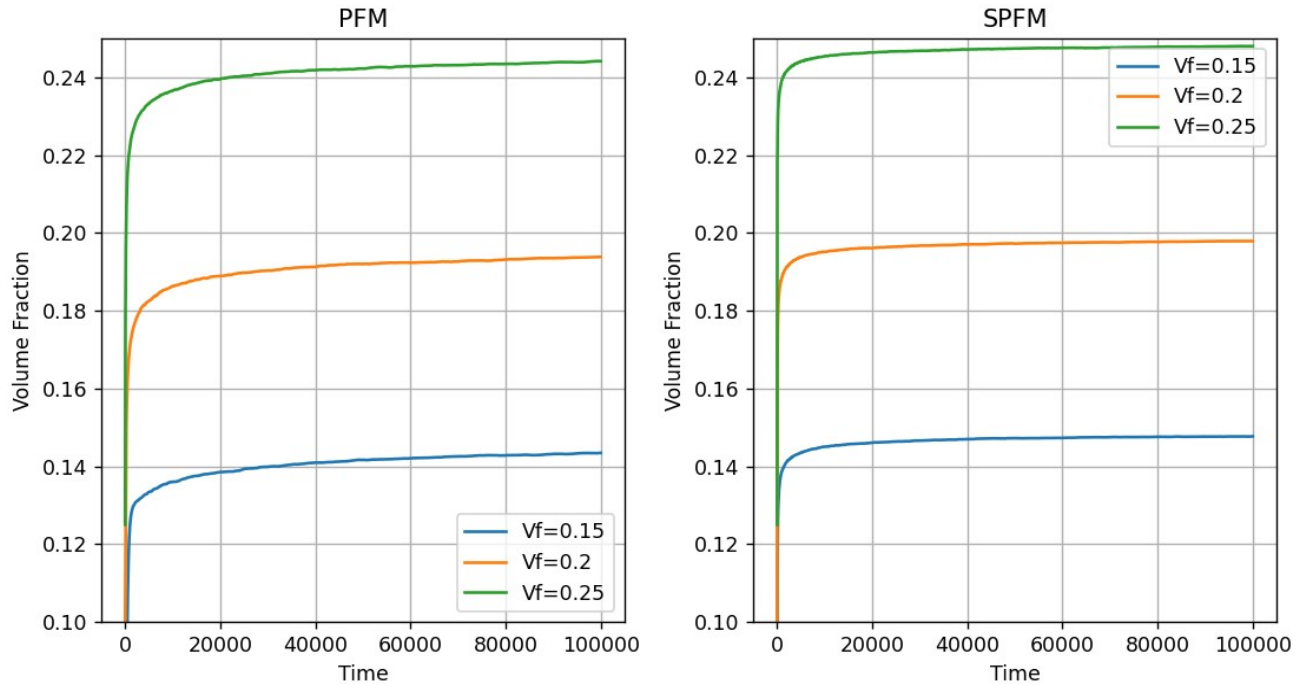
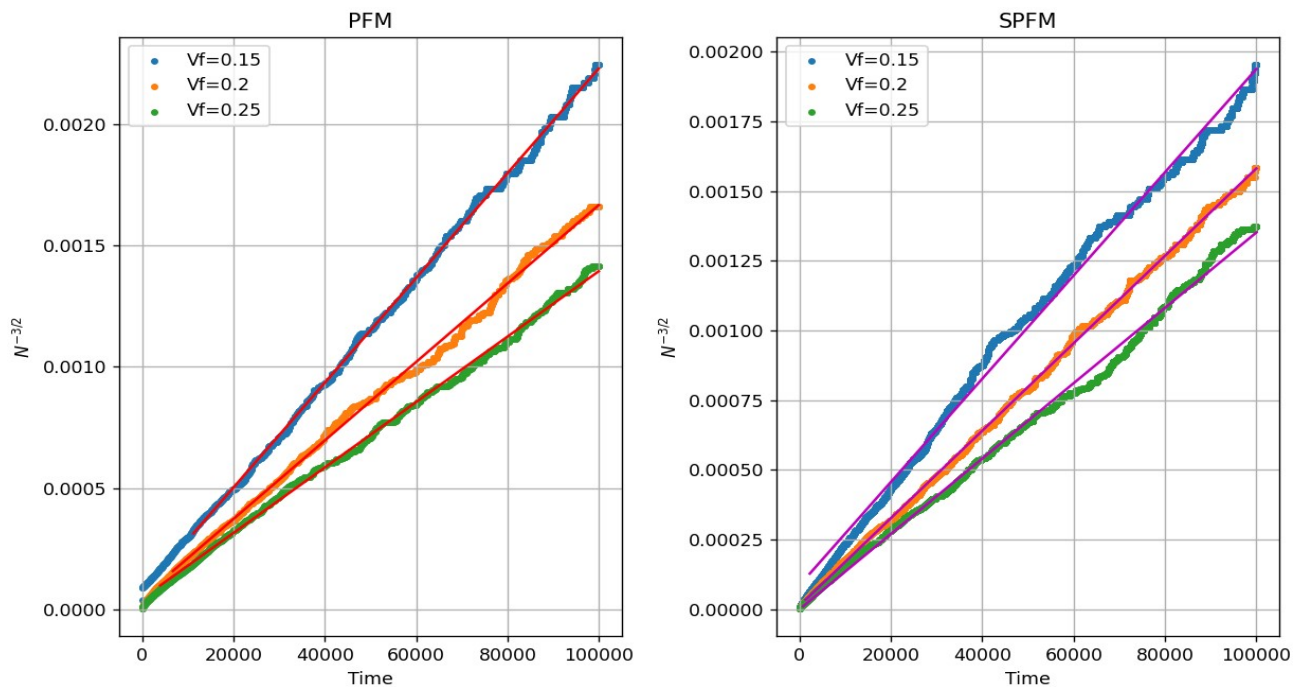
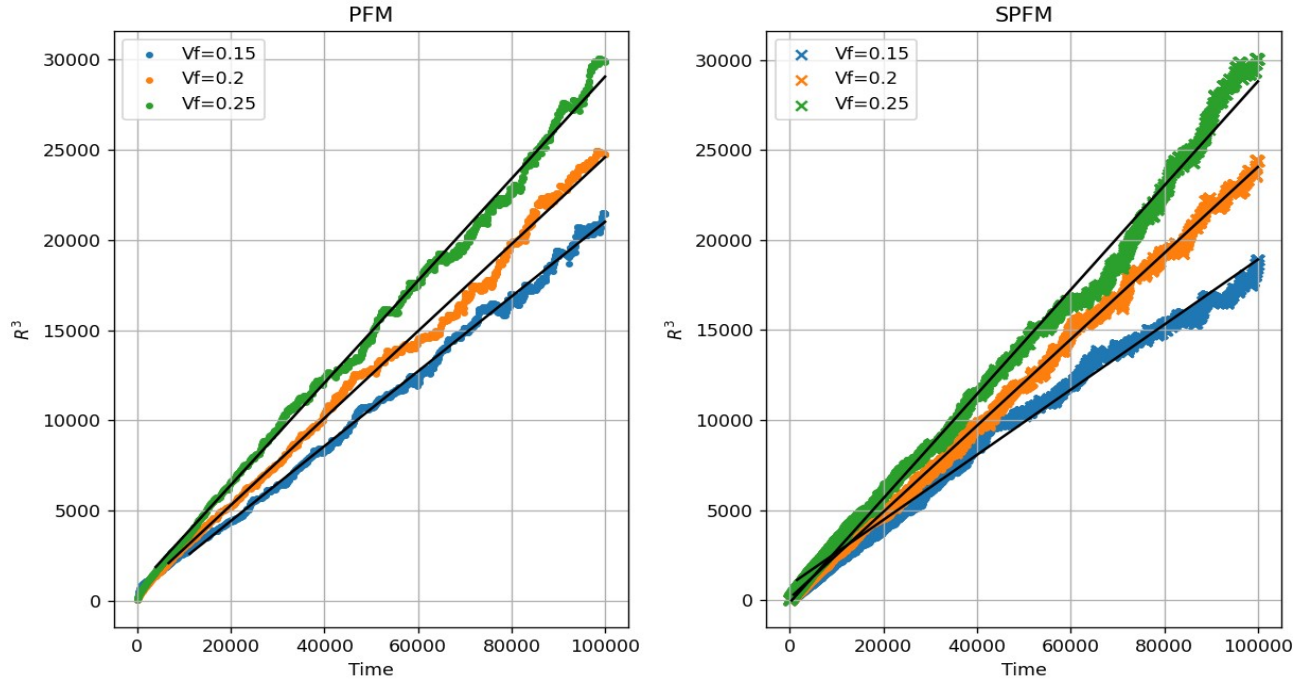


Figure 4.15: Volume fraction vs Time for PFM and Sharp-PFM

Figure 4.16: $N^{-3/2}$ vs Time for PFM and Sharp-PFM

Figure 4.17: R^3 vs Time for PFM and Sharp-PFM

V_f	PFM	S-PFM
0.15	0.21	0.18
0.2	0.24	0.24
0.25	0.28	0.29

Table 4.11: Rate constants in coarsening simulation

The evolution of $Radius^3$ with time is shown in Fig. 4.17. A linear variation of R^3 with time is shown in all the models Fig. 4.17 which happens in coarsening regime [24]. The rate constant k in relation $R^3 = kt$ is calculated by linearly fitting the R^3 vs time time plot from the beginning of coarsening regime and the results are shown in Table 4.11. As seen in table with increasing volume fraction the rate constant increases as well. This result is in accordance with the theoretical prediction by Ardell [25].

In the coarsening regime as volume fraction is constant

$$N\pi R^2 = \text{constant} \quad (4.9)$$

here N is particle density and as R^3 is proportional to time

$$Nt^{2/3} = \text{constant} \quad (4.10)$$

$$N^{-3/2} \alpha \quad t \quad (4.11)$$

The variation of number density is shown in Fig. 4.16. As seen from this plot $N^{-3/2}$ can be seen as varying almost linearly with time in, which is an indication that the microstructure is now in coarsening regime.

For a given volume fraction the coarsening rate is approximately equal for classical and sharp PF models. This is because the chemical potential (interface energy) is matched across models and same atomic mobility parameter. So if the interface energy is doubled then the coarsening rate should also change proportionally. Another simulation is performed with Classical-PFM with A and K as 2 so that the interface energy of a flat interface becomes twice while simultaneously the width does not change. For the volume fraction of 0.2 with these new values the coarsening rate is 0.48 which is exactly double the coarsening rate with A and K as 1. The radius evolution with these new parameters is shown in Fig. 4.18 ,compared to the previous results.

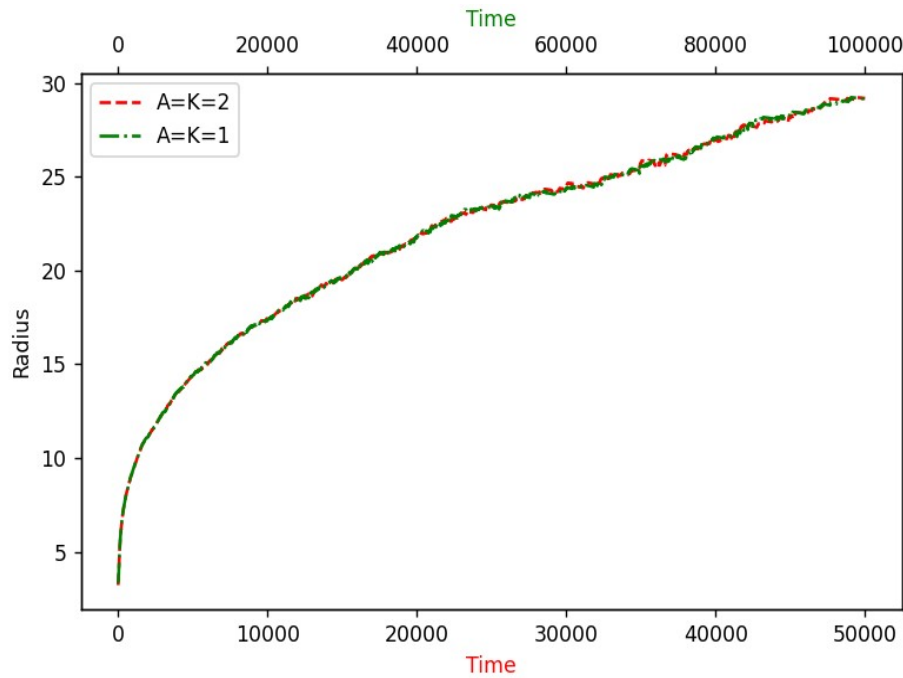


Figure 4.18: Radius vs Time for Classical-PFM for different chemical potential

From above figure it can be seen that in model with $A=K=2$ (red curve) the radius predicted at any time (say t_0) is same as the radius predicted by model with $A=K=1$ (green curve) at time $2t_0$. This also proves that with increasing the interface energy by a certain factor the kinetics are double. In our simulation using Sharp-PFM where the interface energy is doubled a very similar trend is seen in terms of kinetics as observed in Classical-PFM.

This proves that, for a given V_f , coarsening rate for Classical and Sharp PFM is equal because of same interface energy and atomic mobility parameter in both cases.

S-PFM with a higher grid spacing

The Classic-PFM is now represented in a system using a higher grid spacing in Sharp-PFM. For this simulation, the grid spacing for S-PFM is chosen as 2, d/w ratio of 1 and λ is adjusted to 2.264 to get similar interface energy as Classical-PFM. From the starting point of Classical-PFM, which has 1024 grid points in one direction, alternate points are chosen in one direction and assigned to each point in matrix of Sharp-PFM. This is repeated in both the directions of matrix and finally a matrix with 512 grid points in each direction is constructed. With this starting point in Sharp-PFM the system is evolved with Cahn-Hilliard evolution.

The microstructural evolution for a precipitate volume fraction of 0.25 is shown in Fig. 4.20 for both the models at different time steps. It can be seen visually that the radius and number particles in both models at a given time are qualitatively similar. The coarsening rate for Sharp-PFM ($\Delta x = 2$) is 0.3 which is very close to the coarsening rate of Classical-PFM with same volume fraction.

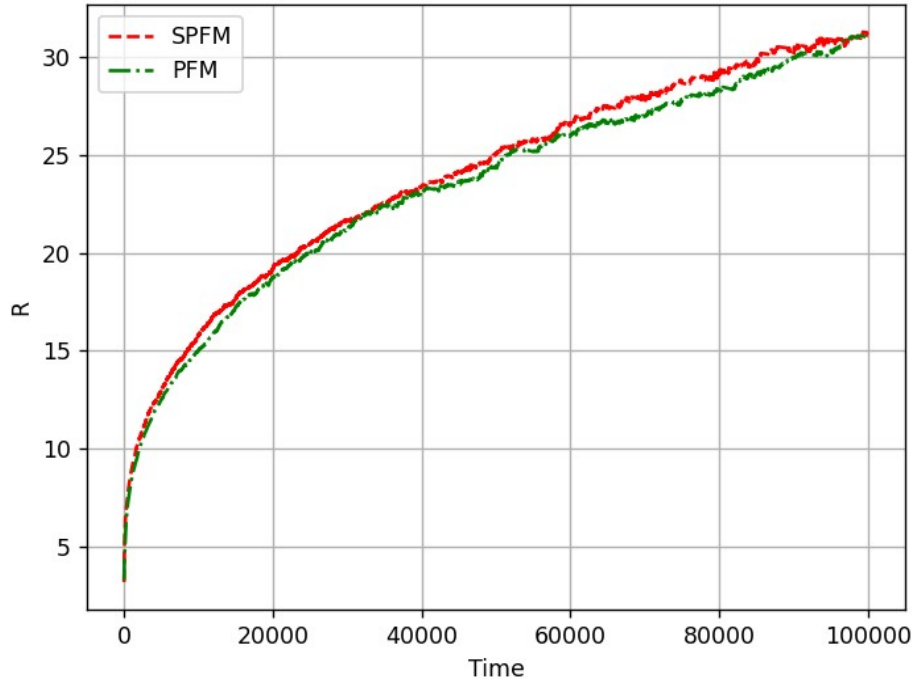


Figure 4.19: Radius vs Time evolution in Classical-PFM ($\Delta x = 1$) and Sharp-PFM ($\Delta x = 2$)

The radius evolution of this Sharp-PFM and Classical-PFM with time is shown in Fig. 4.19. As seen from Fig. 4.19 the radius predicted by Sharp-PFM with smaller number of grid points (512×512) is very close to the radius predicted using Classical-PFM with a higher number of grid points (1024×1024). This might not be possible with Classical-PFM as higher grid spacing leads to grid pinning in Classical-PFM.

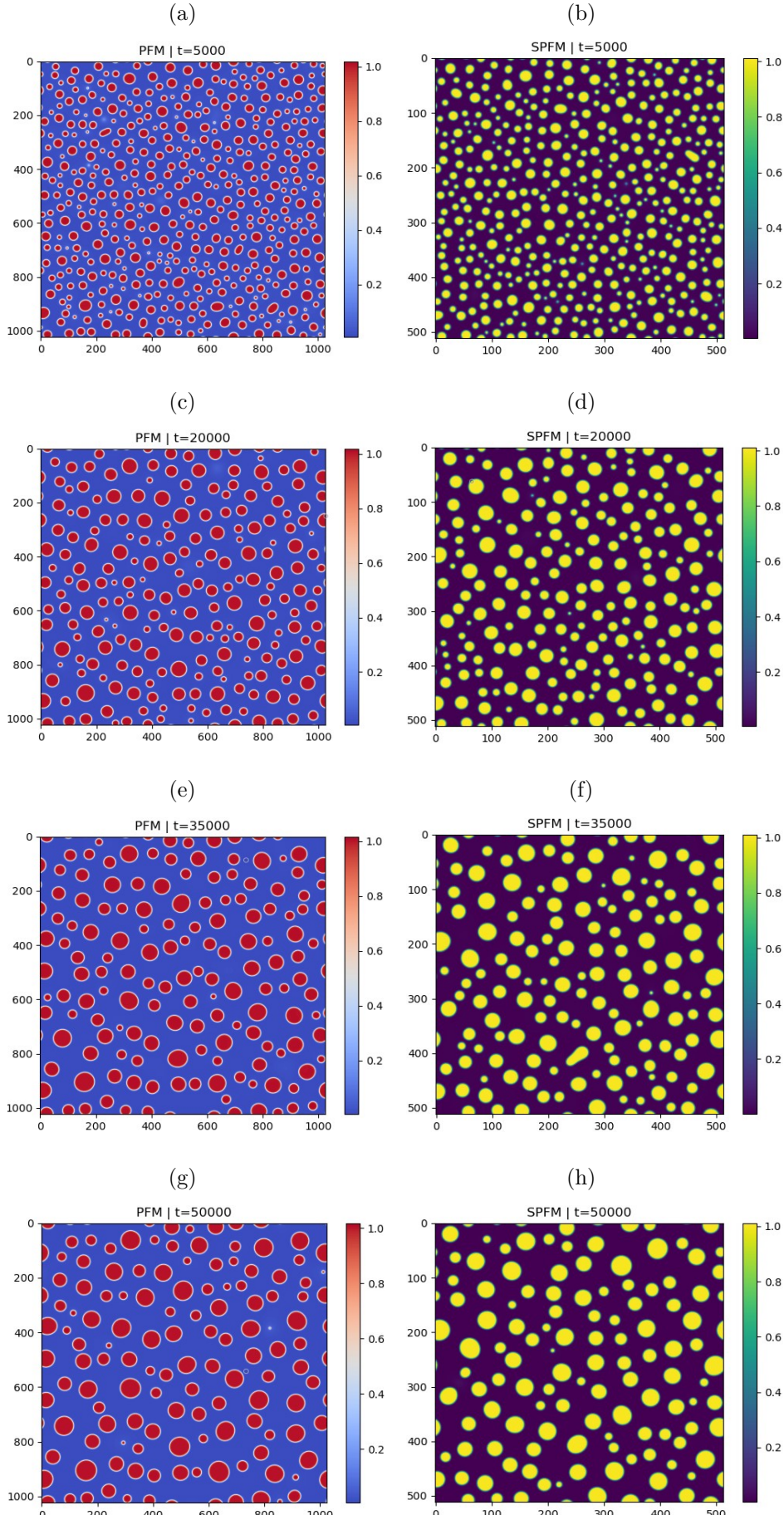


Figure 4.20: Microstructural evolution during coarsening for V_f of 0.25 in Classical-PFM ($\Delta x = 1$) and Sharp-PFM ($\Delta x = 2$) at different time steps.

The computation time (CPU time) required per grid point per time step in Classical-PFM ($\Delta x = 1$) is 1.8×10^{-7} s and for Sharp-PFM ($\Delta x = 2$) is 1.4×10^{-7} s. Also, the number of points in Sharp-PFM were 4 times less. But, the maximum allowable Δt that was taken for a stable simulation was 0.5 in Classical-PFM and 0.1 in Sharp-PFM. These factors effectively make the simulation time in Sharp-PFM and Classical-PFM almost same.

In Cahn-Hilliard evolution using Sharp-PFM we can represent a similar system as Classical-PFM in lesser number of points giving us a good memory advantage but the simulation time remains almost equal. So, Sharp-PFM can be used with Cahn-Hilliard models only when memory is a constraint in simulation but not time. Using Sharp-PFM, 4 times higher number of particles compared to Classical-PFM can be taken in same number of grid points and coarsening can be studied with better statistical results. This will be further helpful in coarsening studies in 3D where this factor is 8 times that of Classical-PFM.

4.5 Limitations

In Sharp-PFM the maximum Δt that could be taken for stability during simulations was found to be less than what can be taken in Classic-PFM with same grid spacing.

Chapter 5

Conclusions

1. Grid pinning is absent in Sharp Phase Field Method at higher grid spacing.
2. In Allen Cahn model
 - (a) In 2D systems a model of Classic-PFM can be represented using a Sharp-PFM model with a higher grid spacing giving good advantage in terms of required computational memory.
 - (b) In 2D systems the Sharp-PFM has very short simulation time compared to Classical-PFM for achieving similar kinetic accuracy.
3. In Cahn Hilliard model
 - (a) For same atomic mobility the critical wavelength is smaller in Sharp-PFM compared to Classical-PFM, during spinodal decomposition.
 - (b) With the same atomic mobility, the Sharp-PFM has a higher growth rate compared to Classic-PFM because of high variation in $\frac{\partial^2 f}{\partial c^2}$ values in Sharp-PFM.
 - (c) In coarsening studies Sharp-PFM can represent same system as Classical-PFM but with higher grid spacing giving good computational memory advantage. The simulation time was same in both models because of lower Δt for stable simulations in Sharp-PFM.
 - (d) Sharp-PFM using Cahn-Hilliard evolution is useful only when memory is a constraint in simulations.
 - (e) In 2D coarsening simulations for same number of grid points, compared to Classical-PFM 4 times higher number of particles can be introduced in Sharp-PFM, hence giving better statistical results.
 - (f) In 3D coarsening studies Sharp-PFM is more attractive as 8 times higher number of particles can be studied compared to Classical-PFM in same number of grid points.

Chapter 6

Future Work

1. Systems which are non-square in 2D should be implemented to understand Sharp-PFM much better.
2. Working on 3D systems with Sharp-PFM to take better advantage of the scale of simulations.
3. Introducing aspects of anisotropy in interfacial energy to understand more how the Sharp-PFM behaves in such cases.
4. Working with Sharp-PFM using GPU computing to realise any more advantages of this method.

Appendix A

Non-Dimensionalisation

All primed quantities are dimensional terms and non-primed ones are non-dimensional terms. The non-dimensional composition from dimensional form is given as

$$c = \frac{c' - c'_m}{c'_p - c'_m} \quad (\text{A.1})$$

$$\frac{\partial c}{\partial c'} = \frac{1}{c'_p - c'_m} \quad (\text{A.2})$$

The chemical potential in dimensional form is given in Eq. A.3

$$\begin{aligned} \mu' &= \frac{1}{N'_v} \frac{\delta F'}{\delta c'} \\ &= \frac{1}{N'_v} \frac{\delta F'}{\delta c} \frac{\delta c}{\delta c'} \\ &= \frac{1}{(c'_p - c'_m)} \frac{\delta F'}{\delta c} \frac{\delta c}{\delta c'} \end{aligned} \quad (\text{A.3})$$

The units of $\frac{\delta F'}{\delta c'}$ is energy per unit volume and that of N'_v is atoms per unit volume. So, the units of μ' is energy/atom. Hence,

$$\begin{aligned} \mu &= \frac{\mu'}{E'} \\ &= \frac{1}{E'} \frac{L'^3}{N_v(c'_p - c'_m)} \frac{\delta F'}{\delta c} \\ &= \frac{1}{E'} \frac{L'^3}{N_v(c'_p - c'_m)} \frac{\delta F}{\delta c} \frac{E'}{L'^3} \\ &= \frac{1}{(c'_p - c'_m) N_v} \frac{\delta F}{\delta c} \end{aligned} \quad (\text{A.4})$$

The Cahn-Hilliard equation in dimensional form is given as

$$\begin{aligned}
\frac{\partial c'}{\partial t'} &= M' \nabla'^2 \mu' \\
\frac{(c'_p - c'_m)}{t'} \frac{\partial c}{\partial t} &= M' \nabla'^2 \mu' \\
\frac{\partial c}{\partial t} &= \frac{M' t'}{(c'_p - c'_m)} \nabla'^2 \mu' \\
&= \frac{M' t'}{L'^2 (c'_p - c'_m)} \nabla^2 \mu' \\
&= \frac{M' t'}{L'^2 (c'_p - c'_m)} \frac{1}{N'_v} \nabla^2 \frac{\delta F'}{\delta c'} \\
&= \frac{M' t'}{L'^2 (c'_p - c'_m)} \frac{L'^3}{N'_v} \nabla^2 \left[\frac{\delta F}{\delta c'} \frac{E'}{L'^3} \right] \\
&= \frac{M' t'}{(c'_p - c'_m)} \frac{L'^3 E'}{L'^5} \nabla^2 \left[\frac{\delta(F/N_v)}{\delta c'} \right] \\
&= \frac{M' t'}{(c'_p - c'_m)} \frac{E'}{L'^2} \nabla^2 \left[\frac{\delta(F/N_v)}{\delta c'} \right] \\
&= \frac{M' t'}{(c'_p - c'_m)} \frac{E'}{L'^2} \nabla^2 \left[\frac{\delta(F/N_v)}{\delta c} \frac{\delta c}{\delta c'} \right] \\
\frac{\partial c}{\partial t} &= \frac{M' t'}{(c'_p - c'_m)^2} \frac{E'}{L'^2} \nabla^2 \left[\frac{\delta(F/N_v)}{\delta c} \right]
\end{aligned} \tag{A.5}$$

The non-dimensional atomic mobility parameter (M) from eqn. A.5 is given as

$$M = \frac{M' t'}{(c'_p - c'_m)^2} \frac{E'}{L'^2} \tag{A.6}$$

Taking $A' = E'$ and $L' = [K'/A']^{1/2}$ makes the non-dimensional parameters A and K unity. The typical characteristic length L' is 1 nm and assuming the typical interface energy is 0.1 J/m^2 . Assuming a Simple Cubic structure and lattice parameter of 4\AA the number of atoms per unit volume (N_v) is $L'^3/(4 \times 10^{-10})^3$. In the classical phase field model, the non-dimensional interface energy is $(1/3)$.

$$\begin{aligned}
\frac{\gamma}{N_v K^{1/2}} &= \frac{1}{3} \\
\gamma &= \frac{L'^3}{3 \times (4 \times 10^{-10})^3}
\end{aligned} \tag{A.7}$$

Since the interfacial energy is scaled with characteristic energy and length as $\gamma' = \gamma(\frac{E'}{L'^2})$, the characteristic energy is

$$\begin{aligned} E' &= \frac{L'^2 \gamma'}{\gamma} \\ &= \frac{L'^2 \gamma' \times 3 \times (4 \times 10^{-10})^3}{L'^3} \\ &= \frac{\gamma' \times 3 \times (4 \times 10^{-10})^3}{L'} \\ E' &= 19.2 \times 10^{-21} J \end{aligned} \quad (\text{A.8})$$

The dimensional atomic mobility parameter (M') is related to dimensional diffusivity as

$$D' = \frac{\partial^2 f'}{\partial c'^2} M' \quad (\text{A.9})$$

Differentiating $f' (= A' c'^2 [1 - c']^2)$ twice with composition at the matrix composition gives us

$$\frac{\partial^2 f'}{\partial c'^2} = \frac{2A}{(c'_p - c'_m)^2} \quad (\text{A.10})$$

Assuming a typical value of 0.1 for $(c'_p - c'_m)$ and $10^{-16} m^2/s$ for D' makes the mobility $M' = 26.042 m^2/(J - s)$. By considering the non-dimensional mobility $M = 1$, the dimensional time is derived as $t' = 0.02$ s from eqn. A.6.

Bibliography

- [1] W. Sun, S. Cui, L. Zhang, Y. Du, and B. Huang, “Phase-field simulation of microstructural evolution of γ precipitate in γ matrix in binary ni-al alloys,” *Procedia Engineering*, vol. 36, pp. 200–206, 2012.
- [2] K. Kim, A. Roy, M. Gururajan, C. Wolverton, and P. Voorhees, “First-principles/phase-field modeling of θ precipitation in al-cu alloys,” *Acta Materialia*, vol. 140, pp. 344–354, 2017.
- [3] G. B. McFadden, “Phase-field models of solidification,” *Contemporary Mathematics*, vol. 306, pp. 107–146, 2002.
- [4] A. Dimokrati, Y. Le Bouar, M. Benyoucef, and A. Finel, “S-pfm model for ideal grain growth,” *Acta Materialia*, vol. 201, pp. 147–157, 2020.
- [5] L.-Q. Chen, “Phase-field models for microstructure evolution,” *Annu. Rev. Mater. Res.*, vol. 16, pp. 113–140, Jan. 2002.
- [6] M. Fleck, F. Schleifer, and U. Glatzel, “Frictionless motion of marginally resolved diffuse interfaces in phase-field modeling,” *arXiv preprint arXiv:1910.05180*, 2019.
- [7] T. Abinandanan and F. Haider, “An extended cahn-hilliard model for interfaces with cubic anisotropy,” *Philosophical Magazine A*, vol. 81, no. 10, pp. 2457–2479, 2001.
- [8] A. Finel, Y. Le Bouar, B. Dabas, B. Appolaire, Y. Yamada, and T. Mohri, “Sharp phase field method,” *Physical review letters*, vol. 121, no. 2, p. 025501, 2018.
- [9] J. W. Cahn and J. E. Hilliard, “Free energy of a nonuniform system. i. interfacial free energy,” *The Journal of chemical physics*, vol. 28, no. 2, pp. 258–267, 1958.
- [10] J. W. Cahn, “On spinodal decomposition,” *Acta metallurgica*, vol. 9, no. 9, pp. 795–801, 1961.
- [11] J. Cahn and S. Allen, “A microscopic theory for domain wall motion and its experimental verification in fe-al alloy domain growth kinetics,” *Le Journal de Physique Colloques*, vol. 38, no. C7, pp. C7–51, 1977.

- [12] L.-Q. Chen and A. Khachaturyan, “Computer simulation of decomposition reactions accompanied by a congruent ordering of the second kind,” *Scripta Metallurgica et materialia*, vol. 25, no. 1, pp. 61–66, 1991.
- [13] R. Mukherjee, T. Abinandanan, and M. Gururajan, “Phase field study of precipitate growth: Effect of misfit strain and interface curvature,” *Acta Materialia*, vol. 57, no. 13, pp. 3947–3954, 2009.
- [14] D. Fan, L.-Q. Chen, and S. Chen, “Effect of grain boundary width on grain growth in a diffuse-interface field model,” *Materials Science and Engineering: A*, vol. 238, no. 1, pp. 78–84, 1997.
- [15] D. Fan and L.-Q. Chen, “Computer simulation of grain growth using a continuum field model,” *Acta Materialia*, vol. 45, no. 2, pp. 611–622, 1997.
- [16] N. Ma, Q. Chen, and Y. Wang, “Implementation of high interfacial energy anisotropy in phase field simulations,” *Scripta materialia*, vol. 54, no. 11, pp. 1919–1924, 2006.
- [17] M. Fleck and F. Schleifer, “Sharp phase-field modeling of isotropic solidification with a super efficient spatial resolution,” *arXiv preprint arXiv:2202.07433*, 2022.
- [18] L. Q. Chen and J. Shen, “Applications of semi-implicit fourier-spectral method to phase field equations,” *Computer Physics Communications*, vol. 108, no. 2-3, pp. 147–158, 1998.
- [19] S. G. Kim, W. T. Kim, and T. Suzuki, “Phase-field model for binary alloys,” *Physical review e*, vol. 60, no. 6, p. 7186, 1999.
- [20] M. Frigo and S. G. Johnson, “The design and implementation of fftw3,” *Proceedings of the IEEE*, vol. 93, no. 2, pp. 216–231. 2005. [Online]. Available: <https://www.fftw.org/>.
- [21] R. Mukherjee, T. Abinandanan, and M. Gururajan, “Precipitate growth with composition-dependent diffusivity: Comparison between theory and phase field simulations,” *Scripta Materialia*, vol. 62, no. 2, pp. 85–88, 2010.
- [22] J. Hoshen and R. Kopelman, “Percolation and cluster distribution. i. cluster multiple labeling technique and critical concentration algorithm,” *Physical Review B*, vol. 14, no. 8, p. 3438, 1976.
- [23] A. Kumar, M. Bhaskar, S. Sarkar, and T. Abinandanan, “Phase field modelling of precipitate coarsening in binary alloys with respect to atomic mobility of solute in the precipitate phase,” *Transactions of the Indian Institute of Metals*, vol. 73, no. 6, pp. 1469–1474, 2020.
- [24] I. M. Lifshitz and V. V. Slyozov, “The kinetics of precipitation from supersaturated solid solutions,” *Journal of physics and chemistry of solids*, vol. 19, no. 1-2, pp. 35–50, 1961.

- [25] A. Ardell, "The effect of volume fraction on particle coarsening: Theoretical considerations," *Acta metallurgica*, vol. 20, no. 1, pp. 61–71, 1972.